# D2.2 (AVHRR): Report on the AVHRR FCDR uncertainty

**Michael Taylor (1), Jonathan Mittaz (1,2), Marine Desmons (1), Emma Woolliams (2)**

(1) University of Reading, (2) National Physical Laboratory

**25th September 2017**

# Contents

# 1 Introduction

## 1.1 Scope

This document is one of the five documents that make up the D2-2 report on traceability chains for FCDRs. Since the original project proposal our thoughts have refined and while this document describes the "sequence of measurement standards and calibrations that is used to relate a measurement result to a reference" (the VIM definition of a traceability chain), it is not presenting this in the form of a chain.

This document provides an overview of the uncertainty analysis for the analysed sensors along with the methods to establish metrological traceability for the developed FCDRs and is specifically about the AVHRR FCDR. Document D2-2a provides an overview of the purposes of these documents and explains the basis of the effects tables.

## 1.2 Version Control

| Version | Reason | Reviewer | Date of Issue |
|---------|--------|----------|---------------|
| 1.a     |        |          |               |
| 1.b     |        |          |               |
| 1.c     |        |          |               |

## 1.3 Applicable and Reference Documents

### 1.3.1 D2-2 set of documents

D2-2a               : Principles behind the FCDR effects table
D2-2 (microwave): Report on the MW FCDR: Uncertainty
D2-2 (HIRS)      : Report on the HIRS FCDR: Uncertainty
D2-2 (AVHRR)   : Report on the AVHRR FCDR: Uncertainty (this document)
D2-2 (MVIRI)    : Report on the MVIRI FCDR: Uncertainty

### 1.3.2 References

Bicknell, W.E. (2000). HgCdTe Detector Responsivity and GOES Instrument Calibration, *GOES Project Report NOAA-3(R-1).*

Doelling, D. R., Bhatt, R., Scarino, B. R., Gopalan, A., Haney, C. O., Minnis, P., & Bedka, K. M. (2016). A Consistent AVHRR Visible Calibration Record Based on Multiple Methods Applicable for the NOAA Degrading Orbits. Part II: Validation. *Journal of Atmospheric and Oceanic Technology*, *33*(11), 2517-2534.

Heidinger, A.K., Straka W,C,, Molling, C.C., Sullivan, J.T. & Wu,X (2010) Deriving an inter-sensor consistent calibration for the AVHRR solar reflectance data record, International Journal of Remote Sensing, 31, 6493-6517 DOI: http://dx.doi.org/10.1080/01431161.2010.496472.

International Vocabulary of Metrology, VIM (2008). Evaluation of measurement data—guide for the expression of uncertainty in measurement. *JCGM* 100: 2008 (GUM 1995 with minor corrections).

Merchant, C, Mittaz, J., Woolliams, E. R., Scanlon, T., Dilo, A. (2015). D2-1: Metrological framework for the development of fundamental climate data records, FIDUCEO Report http://fiduceo.pbworks.com/w/file/97334616/D2_1 FCDR Framework for FCDR Development V1.0.pdf.

Merchant, C. J., Paul, F., Popp, T., Ablain, M., Bontemps, S., Defourny, P., Hollmann, R., Lavergne, T., Laeng, A., de Leeuw, G., Mittaz, J., Poulsen, C., Povey, A. C., Reuter, M., Sathyendranath, S., Sandven, S., Sofieva, V. F., and Wagner, W. (2017). Uncertainty information in climate data records from Earth observation, *Earth System Science Data*, 9, 511-527, https://doi.org/10.5194/essd-9-511-2017.

Mittaz, J. P., Harris, A. R., & Sullivan, J. T. (2009). A physical method for the calibration of the AVHRR/3 thermal IR channels 1: the prelaunch calibration data. *Journal of Atmospheric and Oceanic Technology,* 26(5), 996-1019.

Mittaz, J., & Harris, A. (2011). A physical method for the calibration of the AVHRR/3 thermal IR channels. Part II: An in-orbit comparison of the AVHRR longwave thermal IR channels on board MetOp-A with IASI. *Journal of Atmospheric and Oceanic Technology*, 28(9), 1072-1087.

Mittaz, J. (2011b), The Calibration of the Broadband Infrared Sensors Onboard NOAA Satellites, Proceedings of the GHRSST XII science team meeting, John McIntyre Conference Centre, Edinburgh 27th June - 1st July 2011, 270-276 (https://www.ghrsst.org/meetings/12th-international-ghrsst-science-team-meeting-ghrsst-xii/)

Mittaz, Bali & Harris (2013) The calibration of broad band infrared sensors: Time variable biases and other issues, EUMETSAT Meteorological satellite Conference, Vienna, 16-20 September 2013, https://www.eumetsat.int/website/wcm/idc/idcplg?IdcService=GET_FILE&dDocName=PDF_CONF_P_S8_11_MITTAZ_V&RevisionSelectionMethod=LatestReleased&Rendition=Web

Mittaz (2016) Instrument Noise characterization and the Allan/M-sample variance, FIDUCEO Report http://www.fiduceo.eu/content/instrument-noise-characterization-and-allanm-sample-variance

NASA-GSFC (1996). Performance Specification for the NOAA-K, L, M, N, N' & MetOp Advanced Very High Resolution Radiometer/3, S-480-81, Goddard Space Flight Center, NASA, Greenbelt, Maryland.

Theocharous, E., Theocharous, O. (2006). Practical limit of the accuracy of radiometric measurements using HgCdTe detectors, Applied Optics, 45, 7753-7759.

Trishchenko, A. P., & Li, Z.: (2001). A method for the correction of AVHRR onboard IR calibration in the event of short-term radiative contamination. International Journal of Remote Sensing, 22(17), 3619-3624.

Trishchenko, A. P. (2002). Removing unwanted fluctuations in the AVHRR thermal calibration data using robust techniques. *Journal of Atmospheric and Oceanic Technology*, 19(12), 1939-1954.

Trishchenko, A. P., G. Fedosejevs, L. Zhanqing, and J. Cihlar, 2002: Trends and uncertainties in thermal calibration of AVHRR radiometers onboard NOAA-9 to NOAA-16. *Journal of Geophysical Research*, 107, 4778, doi:10.1029/2002JD002353.

Walton, C. C., J. T. Sullivan, C. R. N. Rao, and M. Weinreb, 1998: Corrections for detector nonlinearities and calibration in- consistencies of the infrared channels of the Advanced Very High Resolution Radiometer. Journal of Geophysical Research, 103, 3323– 3337.

Wang, L. & Cao, C. (2008), On-Orbit Calibration Assessment of AVHRR Longwave Channels on MetOp-A Using IASI, IEEE Transactions on Geoscience and Remote Sensing, 46, 4005 – 4013, DOI:  10.1109/TGRS.2008.2001062.

Weinreb, M. P., Hamilton, G., Brown, S., & Koczor, R. J. (1990). Nonlinearity corrections in calibration of Advanced Very High Resolution Radiometer infrared channels. Journal of Geophysical Research: Oceans, 95(C5), 7381-7388.

Woolliams, E. R. (2014). Uncertainty analysis for filter radiometry based on the uncertainty associated with integrated quantities. International Journal of Thermophysics, 35(6-7), 1353-1365.

Woolliams, E. R., Mittaz, J. P., Merchant, C. J., Dilo, A., & Fox, N. P. (2016). Uncertainty and Correlation in Level 1 and Level 2 Products: A Metrologist's View. In: Living Planet Symposium, Vol. 740, p. 80.

Woolliams, E. R., Hueni, A., Gorroño, J. (2015). Intermediate Uncertainty Analysis for Earth Observation (Instrument Calibration), EMRP-ENV04-D5.2.2_textbook (version 2), http://www.meteoc.org/outreach-training.html.

Wu, X., J. J. Sullivan, J. J., and A. K. Heidinger, A. K. (2010). Operational calibration of the Advanced Very High Resolution Radiometer (AVHRR) visible and near-infrared channels, Canadian Journal of Remote Sensing 36, 602-616.

## 1.4  Glossary

| | |
|---|---|
| AVHRR | Advanced Very High Resolution Radiometer |
| DSV | Deep Space View |
| FCDR | Fundamental Climate Data Record |
| ICT | Internal Calibration Target |
| IR | Infrared |
| IWCT | Internal Warm Calibration Target |
| MetOp | Meteorological Operational satellite |
| NEdT | Noise Equivalent delta Temperature |
| NOAA | National Oceanic and Atmospheric Administration |
| PFM | Pre-Flight Model |
| PRT | Platinum Resistance Thermometer |
| SRF | Spectral Response Function |
| TIROS | Television Infra-Red Observation Satellite |
| VIM | International Vocabulary of Metrology |

Other definitions:

4

"Type A" and "Type B" refer to definitions from the Guide to Uncertainty in Measurement. Type A is based on statistical analysis; Type B is based on expert judgement.

## 2   FIDUCEO effects tables

In FIDUCEO we have defined an effects table which describes:

- the uncertainty associated with a given effect
- the sensitivity coefficient required to propagate uncertainties associated with that effect to uncertainties associated with the measurand (Earth radiance, reflectance or brightness temperature)
- the correlation structure over spatial, temporal and spectral scales for errors from this effect.

The concepts behind the effects tables are described in D2-2a. In this document we provide a discussion of the effects tables and uncertainty propagation for a single instrument series; here the AVHRR FCDR.

## 3   The AVHRR instrument

The Advanced Very High Resolution Radiometer (AVHRR) is a broadband, four or five channel (depending on the model) across-track scanner, that senses in the visible, near-infrared, and thermal infrared portions of the electromagnetic spectrum (see Table 2).

Cross-track scanning is accomplished by a continuously rotating scan mirror (oriented at 45 degrees with respect to the axis of rotation to avoid the variation of polarization effects across the swath) that is directly driven by a motor. The AVHRR flies on-board the National Oceanic and Atmospheric Administration's (NOAA's) Polar Orbiting Environmental Satellites (POES), since 1978 with TIROS-N, which is the first version of the instrument. Each pass of the satellite provides a 2399 km wide swath. The satellite orbits the Earth 14 times each day from 833 km above its surface. The AVHRR instrument detects reflected solar and radiated thermal energy from land, sea, clouds and the atmosphere to provide global imagery (Cracknell, 1997).

Since TIROS-N, there have been 3 instances of AVHRR/1, 6 instances of AVHRR/2 (one of which failed to reach orbit) and 7 instances of AVHRR/3 (see Table 1). Differences between subsequent versions of AVHRR include a more rigorous pre-launch characterization and the addition of a sun shield in the case of AVHRR/3.

*Table 1 A summary of the temporal coverage of the different AVHRR instruments*

| Generation | Satellite Name | Equator Crossing | Start time | End time |
|---|---|---|---|---|
| **AVHRR/1** | TIROS-N | AM | 1978-10-19 | 1980-01-30 |
| **AVHRR/1** | NOAA-6/A | AM | 1979-06-27 | 1986-11-16 |
| **AVHRR/2** | NOAA-7/C | PM | 1981-08-24 | 1986-06-07 |
| **AVHRR/1** | NOAA-8/E | AM | 1983-05-03 | 1985-10-31 |
| **AVHRR/2** | NOAA-9/F | PM | 1985-02-25 | 1994-05-11 |
| **AVHRR/1** | NOAA-10/G | AM | 1986-11-17 | 1991-09-17 |
| **AVHRR/2** | NOAA-11/H | PM | 1988-11-08 | 1994-09-13 |
| **AVHRR/2** | NOAA-12/D | AM | 1991-05-14 | 1994-12-15 |
| **AVHRR/2** | NOAA-13 | | Launch failure | |

| AVHRR/2 | NOAA-14/J | PM | 1994-12-30 | 2007-05-23 |
| AVHRR/3 | NOAA-15/K | AM | 1998-05-13 | Operational |
| AVHRR/3 | NOAA-16/L | PM | 2000-09-21 | 2014-06-09 |
| AVHRR/3 | NOAA-17/M | AM | 2002-06-24 | 2013-04-09 |
| AVHRR/3 | NOAA-18/N | PM | 2005-08-30 | Operational |
| AVHRR/3 | NOAA-19/N' | PM | 2009-06-02 | Operational |
| AVHRR/3 | MetOp-A | AM | 2007-06-20 | Operational |
| AVHRR/3 | MetOp-B | AM | 2013-04-24 | Operational |

*Table 2 Wavelength range for the AVHRR channels*

| Channel | AVHRR/1 | AVHRR/2 | AVHRR/3 | Detector |
|---|---|---|---|---|
| 1 | 0.58-0.68 μm | 0.58-0.68 μm | 0.58-0.68 μm | Si |
| 2 | 0.725-1.1 μm | 0.725-1.1 μm | 0.725-1.1 μm | Si |
| 3a | | | 1.58-1.64 μm | Si |
| 3b | 3.55-3.93 μm | 3.55-3.93 μm | 3.55-3.93 μm | InSb |
| 4 | 10.50-11.50 μm | 10.50-11.50 μm | 10.50-11.50 μm | HgCdTe |
| 5 | Channel 4 repeated | 11.5-12.5 μm | 11.5-12.5 μm | HgCdTe |

The FCDR of interest is for visible and infrared radiances, though this document concentrates mainly on the infrared channels. The thermal channels are calibrated before launch as well as in-flight, using measurements of an internal warm calibration target (IWCT) and of a cold (deep space) target (S). This allows us to evaluate the instrument response as it changes with time. The calibration cycle is undertaken during every full scan, i.e. about 40000 times per orbit. On short time scales (sub-orbital), the calibration results are used to account for the changes in the instrument response associated with variations in the instrument operating temperatures, which vary by ≈3 K around an orbit. On longer time scales (lifetime of the instrument), the instrument response can change because of other factors, such as deterioration of the detectors/optics etc.

The AVHRR is a scanning radiometer that collects pixels as a sequence of scan lines at right angles to the direction of travel of the satellite over the ground. The in-flight calibration procedure of the AVHRR consists of ten measurements (as counts) per scan line when viewing the IWCT and ten measurements per scan line of counts for a space view. Four PRTs measure the temperature of the IWCT and allow an estimate of the spectral radiance from the IWCT to be made using Planck's Law and the estimated emissivity. From the spectral radiance, the channel-integrated spectral radiance from the IWCT is calculated by integrating the spectral radiance across the (assumed known) spectral response function (SRF) of a given channel.

The basic quantity recorded is "counts", a digital number value that relates to the voltage seen over the detector and corresponds to the total incident radiance including instrument self-emission. In operation, all the detectors are actively cooled to a temperature of 105 K to reduce detector noise and increase sensitivity. The electronics have been configured such that the counts reduce with increasing radiance. In order to maintain a dynamic range, the voltage from the space view (or cold target) observations are actively electronically clamped and are used as a reference voltage. This means that the detected signal is implicitly the total radiance observed by the detectors at the time of observation minus the radiance observed by the detectors when viewing space. The recorded counts are the result of a conversion of the analogue detected signal to a 10-bit binary form within the instrument.

While radiances are calibrated in units of mW m$^{-2}$ sr$^{-1}$ cm, measurements are usually converted to Brightness Temperatures (BTs) in units of kelvin. The brightness temperature calculation assumes a monochromatic measurement and a Planckian source. The channel-integrated radiance $L_{ch}(T_b)$ is the weighted average of the black body radiance $L_{BB}(\lambda, T_b)$ at temperature $T_b$ and wavelength $\lambda$ calculated from the Planck function, weighted by the spectral response function of each channel $\xi_{ch}(\lambda)$:

$$L_{ch}(T_b) = \frac{\int \xi_{ch}(\lambda) L_{BB}(\lambda, T_b) \, d\lambda}{\int \xi_{ch}(\lambda) \, d\lambda} \qquad \text{Eq 3-1}$$

Using Eq 3-1, it is straightforward to construct a lookup table to calculate the radiance as a function of brightness temperature or its inverse $T_b(L_{ch})$. Another approach is use "band correction factors" (Weinreb et al., 1990) to convert radiance to brightness temperatures. These use a monochromatic assumption and use a fitted central wavenumber and temperature correction coefficients (usually denoted by *a* and *b*) to closely match the behavior of Eq. 3-1. The full procedure is described in detail by Weinreb et al. (1990).

## 3.1 The AVHRR measurement function

The calibration algorithms of the AVHRR have had numerous incarnations over the lifetime of the sensor (1978 to present). Originally no account was made for the nonlinearity of the 11 and 12µm HgCdTe detectors, whereas subsequent calibration schemes used a range of lookup tables or correction terms to deal with it. The current operational calibration is based on Walton et al. (1998) and consists of a two-step process with a linear radiance first being calculated which is then corrected using a quadratic correction term. As has been pointed out by Mittaz et al. (2009), this formulation is intrinsically problematic. It is also clear that using parameters derived from pre-launch data within this formulation gives rise to significant biases (Wang & Cao 2008, Mittaz & Harris 2011).

An improved calibration equation, from[1] Mittaz & Harris (2011), is:

$$L_E = a_0 + \frac{(\varepsilon + a_1)\tilde{L}_{IWCT} - a_2 - a_3\left(\bar{C}_S - \bar{C}_{IWCT}\right)^2}{\left(\bar{C}_S - \bar{C}_{IWCT}\right)}\left(\bar{C}_S - C_E\right) + a_3\left(\bar{C}_S - C_E\right)^2 + a_4 f(T_{inst}) + 0 \qquad \text{Eq 3-2}$$

where, the terms are:

| | |
|---|---|
| $a_0, a_1, a_2, a_3, a_4$ | Calibration coefficients determined through harmonisation. Note that the $a_2$ term is usually set to zero (see Section 5) |
| $\varepsilon$ | Pre-launch estimated emissivity of the ICT |
| $\tilde{L}_{ICT}$ | Band-integrated radiance of the ICT |
| $C_E$ | Count signal observing the Earth |
| $\bar{C}_S$ | Averaged count signal observing deep space (average of all space-view |

---

[1] With minor further adaptions

| | measurements for this scanline and for 25 scanlines either side) |
|---|---|
| $\bar{C}_{\mathrm{IWCT}}$ | Averaged count signal observing the internal warm calibration target (average of all space-view measurements for this scanline and for 25 scanlines either side) |
| $f\left(T_{\mathrm{inst}}\right)$ | A function for the instrumental temperature that applies to this particular AVHRR instrument and corrects for orbital drift effects (see also Section …). The instrumental temperature used here as a proxy for thermal effects on the satellite is the averaged IWCT temperature over one orbit. |
| +0 | Represents the assumptions underpinning the form of the equation, and in particular the assumption that there is no non-quadratic nonlinearity. |

The band-integrated IWCT radiance is given by

$$\tilde{L}_{\mathrm{ICT}} = \int L_{\mathrm{BB}}\left(\lambda,T_{\mathrm{IWCT}}\right)\xi\left(\lambda\right)\mathrm{d}\lambda \approx \sum_{i} L_{\mathrm{BB}}\left(\lambda_i,T_{\mathrm{IWCT}}\right)\xi\left(\lambda_i\right)\delta_{\lambda i} + 0 \qquad \textit{Eq 3-3}$$

where $\xi\left(\lambda\right)$ is the relative spectral response function, normalised to unit area, $L_{\mathrm{BB}}\left(\lambda,T_{\mathrm{IWCT}}\right)$ represents the Planck radiance for a blackbody at temperature $T_{\mathrm{IWCT}}$ and the integral over wavelength, $\lambda$, is practically realised numerically from tabulated values of the spectral response function at wavelengths $\lambda_i$. The +0 term represents the extent to which this summation does not represent the true integral.

The temperature of the IWCT is calculated from a simple mean of the four temperatures obtained from the four platinum resistance thermometers (PRTs) mounted on the IWCT. Note that this implicitly assumes a planar temperature distribution across the IWCT. If the temperature distribution is more complex (as it likely is) there will be an error introduced by using the simple mean. The PRTs themselves are recorded as a count which is converted to temperature using a calibration equation expressed as a fifth order polynomial. The calibration coefficients for the PRTs were determined pre-launch through comparison with a more accurate thermometer at different temperatures.

## 3.2 Measurement Function Tree Diagram

The measurement function tree diagram for AVHRR is given in Figure 1. The tree is designed to show the sources of uncertainty from their origin through to the uncertainty in the measurand. On the outside of the tree are the origins of the uncertainty which range from those with a physical origin such detector/electronic noise sources (which will be purely random effects) to error sources in the estimate of the internal calibration target (IWCT) radiance which are related to the limited design of the IWCT and which can contain both random (such as noise on the PRT measurements) and systematic (such as errors in PRT calibration) components. Other sources of error are due to the difficulty in our ability to model complex effects such as the corrections required due to solar contamination of the IWCT or the impact of thermal gradients on the imperfect IWCT itself. There are also uncertainties related to errors introduced by our imperfect knowledge of each channels spectral response function. Then there are errors related to effects we cannot directly measure such as the variation in the nonlinearity of the HgCdTe detector due to changes in the photon flux (e.g. Theocharous & Theocharous 2006) which are known to be present but would need the detector itself to be measured in a laboratory to obtain estimates of uncertainty which is impossible as the detector itself has been launched into space. Note that we try to include all possible sources of uncertainty, however small, that is one of the requirements of metrological traceability.
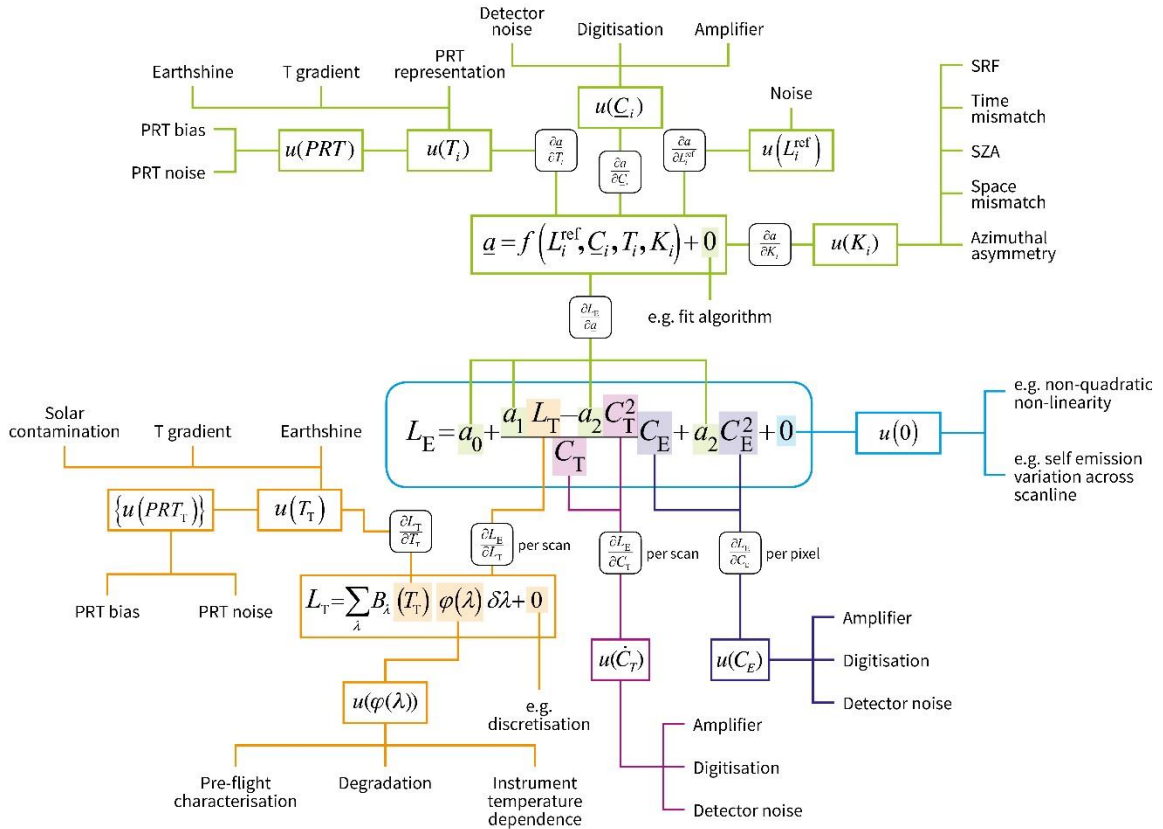
*Figure 1 The measurement function tree for AVHRR. Note the measurement equation is a simplified form where* $C_T = (\overline{C}_S - \overline{C}_{IWCT})$ *and* $C_E = (\overline{C}_S - C_{Earth})$

# 4  A discussion of different terms

In this section we consider the different sources of uncertainty and discuss the error correlation structure for this effect in the different dimensions using the Effects Tables that have been described in D2-2a. A full description of how these effects were evaluated is beyond the scope of this paper, but references are given, or details are provided in the appendices.

## 4.1  Noise in Earth Counts, Averaged Space Counts and Averaged IWCT Counts

Each detector has its own noise characteristics. There are a number of different noise sources that may be applicable for the AVHRR detectors including thermal noise (related to the detector temperature which as mentioned above for the AVHRR is held constant), shot noise (from statistical variations in the number of carriers which is itself a function of flux), 1/f noise from surface effects, noise generated by the electronics etc. We also have a range of detectors (Silicon for the visible/NIR channels, InSb for the 3.7µm channel and HdCdTe for the 11/12µm channels) which will each have their own noise characteristics.

It is actually quite difficult to measure the noise directly for the AVHRR. This is because observations of known sources (either space or the IWCT) only take 10 measurements at a time and, due to the variation of instrument temperature around an orbit, the total flux between measurements is not strictly constant. Further, the on-board digitisation is itself can be of the order

of the noise, which again makes an accurate measurement of the detector noise difficult. The Earth Count noise is even harder to estimate because it is difficult to find Earth scenes that are sufficiently uniform to estimate any Earth Count noise. This noise is therefore estimated as the larger of the noise levels observed from the 10 IWCT or 10 space measurements (and just the space measurements for the visible channels). A further discussion is given in Appendix A.1.

The Earth count is observed per pixel and therefore any noise associated with it will generally be independent from one pixel to another (it is a purely random effect). There may be a small exception to this rule for some AVHRR instruments where there has been observed cross-talk over time and between channels, see Appendix A.1 for more information.

The Space and IWCT counts are, however, determined once per scanline and averaged as a simple rolling average across an averaging window of N scanlines (N/2 before and N/2 after) where N is sensor dependent and varies from 51 to 101. This means that all pixels on a scanline have a fully correlated error associated with IWCT and Space observation noise and that the correlation from one scanline to another falls off as a triangle (see D2-2a). For most AVHRR instruments there is no correlation from spectral channel to spectral channel, though for the earliest AVHRR instrument on board TIROS-N there is some observed correlation between channels (see Appendix A.1). While the TIROS-N is not included in the time range specified for the AVHRR FCDR, it is discussed here as it has provided physical understanding of, for example, electronics noise on other sensors that are included in the FCDR.

The effects tables for AVHRR counts are given in Table 3.

*Table 3 Effects tables for the Earth, averaged-Space and averaged-IWCT counts*

| Table descriptor | | | | |
|---|---|---|---|---|
| Name of effect | | Earth Count Noise | Averaged Space Count Noise | Averaged IWCT Count Noise |
| Affected term in measurement function | | $C_E$ | $\bar{C}_S$ | $\bar{C}_{IWCT}$ |
| Instruments in the series affected | | All | All | All |
| Correlation type and form | **Pixel-to-pixel [pixels]** | Random* | Rectangular Absolute | Rectangular Absolute |
| | **from scanline to scanline [scanlines]** | Random* | Triangular | Triangular |
| | **between images [images]** | N/A | N/A | N/A |
| | **Between orbits [orbit]** | Random | Random | Random |
| | **Over time [time]** | Random | Random | Random |
| Correlation scale | **Pixel-to-pixel [pixels]** | [0] | $[-\infty, +\infty]$ | $[-\infty, +\infty]$ |
| | **from scanline to** | [0] | n = 51 | n = 51 |

| | | | | |
|---|---|---|---|---|
| | scanline [scanlines] | | | |
| | between images [images] | N/A | N/A | N/A |
| | Between orbits [orbit] | [0] | [0] | [0] |
| | Over time [time] | [0] | [0] | [0] |
| Channels/ bands | List of channels / bands affected | All | All | All |
| | Correlation coefficient matrix | Identity matrix (1s down diagonal only)* | Identity matrix (1s down diagonal only)* | Identity matrix (1s down diagonal only)* |
| Uncertainty | PDF shape | Digitised Gaussian | Digitised Gaussian | Digitised Gaussian |
| | units | Counts | Counts | Counts |
| | magnitude | Provided per pixel | Provided per scanline? | Provided per scanline? |
| Sensitivity coefficient | | $\dfrac{\partial L_E}{\partial C_E}$, Eq 4-1 | $\dfrac{\partial L_E}{\partial \bar{C}_S}$, Eq 4-2 | $\dfrac{\partial L_E}{\partial \bar{C}_{IWCT}}$, Eq 4-3 |

*For Tiros-N where there is cross-channel correlation and some pixel-to-pixel correlation in the noise, the correlation form is not random for the Earth counts and there are off-diagonal elements to the channel-to-channel correlation coefficient matrix.*

The sensitivity coefficients are:

$$\frac{\partial L_E}{\partial C_E} = -\frac{\left(\varepsilon + a_1\right)\tilde{L}_{IWCT} - a_2 - a_3\left(\bar{C}_S - C_{IWCT}\right)^2}{\left(\bar{C}_S - \bar{C}_{IWCT}\right)} - 2a_3\left(\bar{C}_S - C_E\right).$$

<div style="text-align:right">*Eq 4-1*</div>

$$\frac{\partial L_E}{\partial \bar{C}_S} = \frac{\left(\varepsilon + a_1\right)\tilde{L}_{IWCT} - a_2 - a_3\left(\bar{C}_S - \bar{C}_{IWCT}\right)^2}{\left(\bar{C}_S - \bar{C}_{IWCT}\right)} - \frac{\left(\bar{C}_S - C_E\right)}{\left(\bar{C}_S - \bar{C}_{IWCT}\right)}\left[\frac{\left(\varepsilon + a_1\right)\tilde{L}_{IWCT} - a_2 - a_3\left(\bar{C}_S - \bar{C}_{IWCT}\right)^2}{\left(\bar{C}_S - \bar{C}_{IWCT}\right)} + 2a_3\left(\bar{C}_S - \bar{C}_{IWCT}\right)\right] + 2a_3\left(\bar{C}_S - C_E\right)$$

<div style="text-align:right">*Eq 4-2*</div>

$$\frac{\partial L_E}{\partial \bar{C}_{IWCT}} = \left(\bar{C}_S - C_E\right)\left[\frac{\left(\varepsilon + a_1\right)\tilde{L}_{IWCT} - a_2 - a_3\left(\bar{C}_S - \bar{C}_{IWCT}\right)^2}{\left(\bar{C}_S - \bar{C}_{IWCT}\right)^2} + a_3\right]$$

<div style="text-align:right">*Eq 4-3*</div>

## 4.2  Spectral response function

The spectral response functions of the different channels were determined pre-launch through an experimental characterisation and are defined by measurements at discrete wavelengths. The

spectral response function is most significantly used in determining the band-integrated radiance of the IWCT and in determining the brightness temperature from the measured radiance.

The spectral response function is generally parametrized during pre-launch testing but the level of detail and accuracy can be variable over time. In the case of the AVHRR, the quality varies over time for a fairly meagre 20 measurements per SRF for the early AVHRRs, up to more than 200 listed values for the AVHRR/3 sensors. There is also always the possibility for a difference between measurements. One example is for NOAA-16 where the end-to-end measurements for the 12μm channel are different from the predicted values based on the responses of the individual optical components provided by the manufacturers. While the piece-part SRFs match reasonably well for the 3.7μm and 11μm channels, there is a clear discrepancy in the case of the 12μm channel (see Mittaz et al. 2009). Which is closer to the truth is, however, unknown at present. Apart from simple measurement errors there is also the possibility of changes in the SRF from pre-launch to in-orbit. This is especially apparent for channels that sit on an absorption lines. Within window channel regions such as are covered by the AVHRR IR channels the situation is not as clear cut as small variations in the SRF have only a small impact on the brightness temperatures as well as the fact that the fitted nonlinearity and a shift to the SRF are correlated (see Mittaz et al., 2009). This means that it is impossible to separate out an SRF shift from a change in the nonlinearity directly.

There are different types of uncertainty that are likely to have affected the original calibration of the spectral response function. In addition, the spectral response function is likely to have changed in orbit due to degradation of optical components, temperature sensitivities of the filters and any mismatch in optical illumination conditions (particularly angular) between calibration and use. These will have caused the following types of error:

- A systematic radiometric error in the SRF. Any error that applies equally (in a relative sense) to all wavelengths will effectively "cancel out" as the SRF used is the normalised SRF.
- A random radiometric error in the SRF. The effect of random noise in the SRF estimate that is random from one discrete wavelength value to the next, will be minimised through the spectral integration, if enough discrete values are combined in that integration.
- Any error that affects the width of the SRF and/or which is asymmetrical across the SRF (for example faster degradation at shorter wavelengths than longer wavelengths) will be significant
- Any systematic bias of the wavelength scale (a shift to shorter or longer wavelengths) will be significant.

In the current pre-beta easy FCDR the SRF is the pre-launch SRF and no component of uncertainty has been assigned (see Appendix A.2). Due to the correlation between the nonlinearity and SRF part of the SRF error will be removed during the non-linear coefficient harmonization but further work is needed both on if an update to the SRF is needed as well as to understand the implication for brightness temperature and whether an erroneous SRF will partially cancel out for some spectral bands where the scenes have a similar spectral shape to the IWCT.

The only error term that will be considered in an effects table is a systematic wavelength shift. There is no correlation in the shift between channels, but the shift is considered identical for all measurements. It is therefore fully systematic, although the sensitivity coefficient will depend on local conditions.

*Table 4 Effects tables for the SRF, considering a spectral shift*

| Table descriptor | | |
|---|---|---|
| Name of effect | | Spectral response function wavelength shift |
| Affected term in measurement function | | $\xi(\lambda) \equiv \xi(\lambda + \delta_\lambda)$ |
| Instruments in the series affected | | All |
| Correlation type and form | **Pixel-to-pixel [pixels]** | Rectangular absolute |
| | **from scanline to scanline [scanlines]** | Rectangular absolute |
| | **between images [images]** | Rectangular absolute |
| | **Between orbits [orbit]** | Rectangular absolute |
| | **Over time [time]** | Rectangular absolute |
| Correlation scale | **Pixel-to-pixel [pixels]** | $[-\infty, +\infty]$ |
| | **from scanline to scanline [scanlines]** | $[-\infty, +\infty]$ |
| | **between images [images]** | $[-\infty, +\infty]$ |
| | **Between orbits [orbit]** | $[-\infty, +\infty]$ |
| | **Over time [time]** | $[-\infty, +\infty]$ |
| Channels/bands | **List of channels / bands affected** | All |
| | **Correlation coefficient matrix** | Identity Matrix (no correlation) |
| Uncertainty | **PDF shape** | Gaussian |
| | **Units** | μm |
| | **magnitude** | Provided as a single value based on sensitivity analysis |
| Sensitivity coefficient | | See **Error! Reference source not found.** and **Error! Reference source not found.** |

## 4.3  IWCT Radiance effects

The IWCT radiance is calculated from **Error! Reference source not found.** assuming that the IWCT is a grey body with an emissivity $\varepsilon + a_3$ for a specific channel, and a temperature given by,

$$T_{\text{IWCT}} = \left( \frac{1}{N} \sum_i T_{\text{PRT},i} \right) + 0$$

*Eq 4-4*

As the simple mean of temperatures $T_{\mathrm{PRT},i}$ measured by the $N=4$ PRTs. The +0 here represents the assumption that the mean PRT signal is equal to the temperature of the IWCT averaged over the field of view of the radiometer. As well as the SRF wavelength shift, the band-integrated radiance of the IWCT is affected by the following components:

- Noise in individual PRT counts
- Systematic calibration bias of the PRTs
- Difference between radiant surface temperature at PRT location (front surface) and PRT measurement location (back of IWCT)
- Emissivity of IWCT
- Representativeness of the mean of the PRTs to the observed OWCT temperature
- Solar contamination of the IWCT

As these have different correlation structures they must be considered separately. Solar contamination and Earthshine are considered in the next section, Section 4.4).

The noise in the PRT counts is a structured random effect, it is random from one measurement to the next, but since the determined IWCT radiance is used for all pixels in a scanline and is averaged over several scanlines in a rolling average, the error in the IWCT radiance due to noise in the PRT measurements has a full correlation within a scanline and a triangular correlation from scanline to scanline. Because the noise in the individual PRTs are independent from one another, we can determine the uncertainty associated with noise in the mean PRT signal, which will be the noise in any individual PRT divided by $\sqrt{N}$. The noise associated with each individual PRT was investigated (Appendix A3.1). It is that noise that is included in the table above. Here the original noise is in counts but it is provided as a temperature error in kelvin.

The systematic calibration bias of the PRTs comes from the accuracy of the original PRT calibration, from any post-calibration drift and from the offset of the PRTs from the front surface of the IWCT. This is a fully systematic uncertainty component. The uncertainty is expressed in kelvin. Note that we do not consider uncertainties in the calibration coefficients for the fifth order polynomial used to convert counts to temperature. This is because those coefficients will be correlated and were determined from a temperature calibration and therefore it is better to think of uncertainties in terms of temperature. The uncertainty associated with the original calibration is treated as an effect of order 0.1 K, based on a conversation with PRT experts at NPL.

Since the PRTs are attached to the baseplate, which the IWCT sits on, the PRT is not measuring the temperature of the IWCT emitting surface itself but is measuring the base of the metal that makes up the IWCT. There is therefore the likelihood of an error between the radiant temperature at the location measured by the PRT and the PRT measured temperature. This error is very difficult to estimate given that no pre-launch measurements were made at the time of such an effect. An estimate of this has been made by Trishchenko et al. (2002) on the basis of the time variability of the measurements but without another study it is not clear if the effect looked at by Trishchenko et al. (2002) was related to a PRT/IWCT measurement issue or was related to problems with the operational calibration algorithm itself which has been shown to be physically wrong (e.g. Mittaz, Harris & Sullivan, 2009).

Uncertainty in the emissivity of the IWCT is not considered. This is because the $a_3$ term, determined during harmonisation, is designed to correct any gross emissivity error. What has not been determined is if the IWCT emissivity changes over time due to degradation but the detection of such an effect is going to be very difficult if not impossible. So we are assuming in the harmonization process that the emissivity is time invariant.

The mean PRT measurement will not be representative of the observed temperature by the AVHRR instrument if there are non-linear thermal gradients across the IWCT. To estimate the possible extent of this, a study was performed (Appendix A.3.2) to understand the possible magnitude of error due to thermal gradients. This studied showed that there were non-planar gradients across the IWCT and that these change over time; both short term (within an orbit) and over the longer term as the thermal environment becomes more extreme following orbital drifts. This effect will be correlated for relatively nearby scanlines (within an orbit and for similar orbital positions from one orbit to the next), but will be random over longer timescales and for points at different parts of the orbit. In Appendix A3.2 we analyse the scale of these correlations along scanlines and across orbits. In particular, we looked at the variation of the correlations at different temporal scales for both AVHRR/3 sensors onboard MetOp-A and NOAA-18, and also for the older AVHRR/1 sensor onboard NOAA-8 and the AVHRR/2 sensor onboard NOAA-7.

Effects tables for these effects are given below. Note that because the IWCT temperature is calculated from the PRT signals and the IWCT band-integrated radiance is calculated for a specific channel from this temperature, all channels have a common error correlation due to these effects.

*Table 5 Effects tables for the IWCT band-integrated radiance*

| Table descriptor | | | | |
|---|---|---|---|---|
| Name of effect | | PRT count noise | PRT bias and offset between baseplate and IWCT temperatures | PRT representativeness (thermal gradients) |
| Affected term in measurement function | | $\tilde{L}_{IWCT}$ | $\tilde{L}_{IWCT}$ | $\tilde{L}_{IWCT}$ |
| Instruments in the series affected | | All | All | All |
| Correlation type and form | **Pixel-to-pixel [pixels]** | Rectangular Absolute | Rectangular Absolute | Rectangular Absolute |
| | **from scanline to scanline [scanlines]** | Triangular | Rectangular Absolute | Truncated Gaussian |
| | **between images [images]** | N/A | N/A | N/A |
| | **Between orbits [orbit]** | Random | Rectangular Absolute | Truncated Gaussian |
| | **Over time** | Random | Rectangular | Random |

| | | | Absolute | |
|---|---|---|---|---|
| | **[time]** | | | |
| Correlation scale | **Pixel-to-pixel [pixels]** | $[-\infty,+\infty]$ | $[-\infty,+\infty]$ | $[-\infty,+\infty]$ |
| | **from scanline to scanline [scanlines]** | n = 51 | $[-\infty,+\infty]$ | A function will be provided but we expect the correlation length to be in the order of some hundreds of scanlines |
| | **between images [images]** | N/A | N/A | N/A |
| | **Between orbits [orbit]** | [0] | $[-\infty,+\infty]$ | Strongly correlated and will be quantified via a correlation coefficient as a function of time |
| | **Over time [time]** | [0] | $[-\infty,+\infty]$ | A function will be provided which will be sensor specific |
| Channels/ bands | **List of channels / bands affected** | All | All | All |
| | **Correlation coefficient matrix** | Matrix of 1s everywhere | Matrix of 1s everywhere | Matrix of 1s everywhere |
| Uncertainty | **PDF shape** | Gaussian | Gaussian | Rectangular |
| | **units** | Counts (kelvin) | kelvin | kelvin |
| | **magnitude** | Provided per orbit? Or as a single value for all time? This should be uncertainty associated with the average PRT count due to noise individual counts. | 0.1 K everywhere | A function will be provided but it is expected that it will be of the order of 1-2K for several of the sensors. |
| Sensitivity coefficient | | $\dfrac{\partial L_{\mathrm{E}}}{\partial \bar{C}_{\mathrm{PRT}}}$ , | $\dfrac{\partial L_{\mathrm{E}}}{\partial T_{\mathrm{IWCT}}}$ | $\dfrac{\partial L_{\mathrm{E}}}{\partial T_{\mathrm{IWCT}}}$ |

We can write, with a chain rule:

$$\frac{\partial L_{\mathrm{E}}}{\partial T_{\mathrm{IWCT}}} = \frac{\partial L_{\mathrm{E}}}{\partial \tilde{L}_{\mathrm{IWCT}}} \frac{\partial \tilde{L}_{\mathrm{IWCT}}}{\partial T_{\mathrm{IWCT}}} \qquad\qquad Eq\ 4\text{-}5$$

where,

$$\frac{\partial L_{\text{E}}}{\partial \tilde{L}_{\text{IWCT}}} = \frac{\left(\varepsilon + a_1\right)}{\left(\bar{C}_{\text{S}} - \bar{C}_{\text{IWCT}}\right)} .$$

*Eq 4-6*

$$\frac{\partial \tilde{L}_{\text{IWCT}}}{\partial T_{\text{IWCT}}} = \sum_i \xi\left(\lambda_i\right) \delta_{\lambda i} \left.\frac{\partial L_{\text{BB}}}{\partial T_{\text{IWCT}}}\right|_{\left(\lambda_i, T_{\text{IWCT}}\right)}$$

*Eq 4-7*

$$\left.\frac{\partial L_{\text{BB}}}{\partial T_{\text{IWCT}}}\right|_{\left(\lambda_i, T_{\text{IWCT}}\right)} = \frac{L_{\text{BB}}\left(\lambda_i, T_{\text{IWCT}}\right) hc}{\lambda_i k_{\text{B}} T_{\text{IWCT}}^2 \left(1 - \exp\left[-hc / \lambda_i k_{\text{B}} T_{\text{IWCT}}\right]\right)}$$

*Eq 4-8*

## 4.4  Solar contamination and Earth shine

### 4.4.1  Solar contamination

There are points in the orbit where the sun shines (directly or indirectly) onto the IWCT. This has two effects:

- In the 3.7 µm channel sunlight is reflected off the IWCT into the detector.
- For all channels – sunlight heats the IWCT in a non-even way which may mean that the radiance calculated from the average of the four PRT readings is not representative of the measured radiance by the detector.

A second effect relates to the "PRT representativeness (thermal gradients)" effect described above and is covered by that effects table (the uncertainty associated with thermal gradients will be larger for scanlines affected by solar contamination).

The reflected sunlight must, however, be considered separately for the 3.7µm channel. This is an effect that is under investigation, some comments are given in A.3.3. It should, however, be noted that the error introduced by the solar contamination is not the signal introduced by the solar radiation but is the error introduced by having to model the underlying gain variation for the periods where the solar radiance is significant. The effect will only affect the 3.7µm channel and so there is no correlation between channels. For this channel the effect will be common for the same time in successive orbits for orbits that are close in time. In this case the solar contamination is identical from orbit to orbit so there is going to be a close to 100% correlation for impacted scanlines. On longer timescales, there is evolution in where the solar contamination is seen which can be seen in the variations in the number of scan lines impacted. See appendix A3.3 for more details.

### 4.4.2  Earth shine

The IWCT is also contaminated by light from the Earth reaching the IWCT. In the 3.7µm channel this includes both sunlight reflected off the Earth and Earth-emitted light. For the other channels, it is from Earth-emitted light. This effect has also not been considered in detail and therefore the effects table given below is considered a first-draft.

### 4.4.3  Effects tables for Solar contamination and Earth shine

*Table 6 Effects tables for the IWCT band-integrated radiance due to solar contamination and Earth shine*

Table descriptor

| Name of effect | | Solar contamination | Earth shine |
|---|---|---|---|
| Affected term in measurement function | | $\tilde{L}_{\text{IWCT}}$ | $\tilde{L}_{\text{IWCT}}$ |
| Instruments in the series affected | | All | All |
| Correlation type and form | Pixel-to-pixel [pixels] | Rectangular Absolute | Rectangular Absolute |
| | from scanline to scanline [scanlines] | Truncated Gaussian | Rectangular Absolute |
| | between images [images] | N/A | N/A |
| | Between orbits [orbit] | Rectangular Absolute | Rectangular Absolute |
| | Over time [time] | Function of difference between number of scanlines impacted by effect | Rectangular Absolute |
| Correlation scale | Pixel-to-pixel [pixels] | $\left[-\infty, +\infty\right]$ | $\left[-\infty, +\infty\right]$ |
| | from scanline to scanline [scanlines] | Function relating to solar contamination modelling. | $\left[-\infty, +\infty\right]$ |
| | between images [images] | N/A | N/A |
| | Between orbits [orbit] | 100% correlation for impacted scanlines | $\left[-\infty, +\infty\right]$ |
| | Over time [time] | Depends on the variation in the effect and will be modelled by looking at the observed characteristics | $\left[-\infty, +\infty\right]$ |
| Channels/ bands | List of channels / bands affected | 3.7 μm only | All |

| | | N/A | Probably fully correlated? |
|---|---|---|---|
| | **Correlation coefficient matrix** | N/A | Probably fully correlated? |
| **Uncertainty** | **PDF shape** | Gaussian | Gaussian |
| | **units** | $W\ m^{-2}\ sr^{-1}$ | $W\ m^{-2}\ sr^{-1}$ |
| | **magnitude** | A model of the uncertainty will be provided | TBD |
| Sensitivity coefficient | | $\dfrac{\partial L_E}{\partial L_{Solar}}$ , | $\dfrac{\partial L_E}{\partial L_{EarthShine}}$ |

The sensitivity coefficients are not yet known as we have not finalized a model for these effects. We also do not have a complete estimate of the correlation structure but will be something like 100% correlation for adjacent orbits for those scanlines with a detected solar contamination flag set since the solar contamination will be at the same point in the orbit with a very similar level. On longer timescales, the correlation between the errors will become less as the configuration of the satellite to Sun angle changes. This has both a yearly cycle and can have a longer-term component due to orbital drift. Examples of the time evolution of the number of scanlines is shown below and it is this sort of information which can be used to estimate the variation in the correlation coefficients on longer timescales.
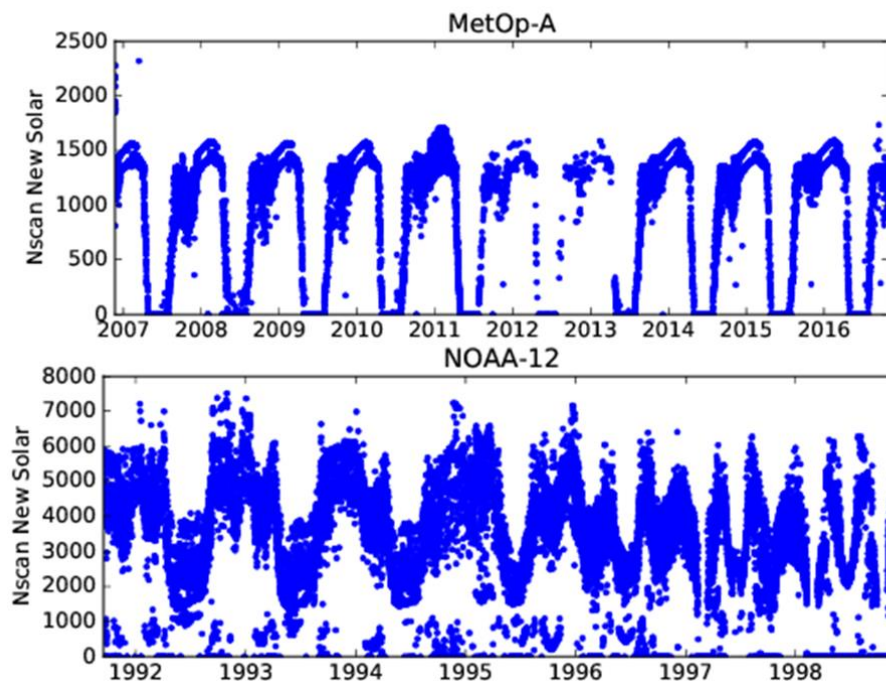


*Figure 2 Number of solar contaminated scan lines detected per orbit for MetOp-A and NOAA-12 using the new solar contamination algorithm (see Appendix). MetOp-A which is kept in a fixed orbit has a very regular yearly cycle of solar events whereas NOAA-12 is more variable. This information will be used as part of the model of the correlation structure for the solar contamination effect table.*

## 4.5 Thermal environment bias

One of the long term biases seen in the AVHRR is related to the overall thermal environment of the sensor and how that environment changes over time as the satellite orbit changes. First noticed in a characteristic SST bias seen relative to drifting buoys in NOAA-16 (Mittaz 2011b) the bias is strongly correlated with the IWCT temperature and seems best correlated when considering the orbital average of the IWCT temperature which we call the instrument temperature ($T_{Instr}$). It is, however, important the realise that $T_{Instr}$ is actually only a crude indicator of the complex and variable thermal structure of the AVHRR instrument that is the true cause of the variable bias and therefore can only be thought of as a proxy measurement which is correlated to some extent with the true source of the bias. The physical origin of the bias is due to the different views (space view, IWCT view and Earth view) seeing different amounts of straylight from different parts of the sensor. Because the part of the sensor seen by the different views are going to be different and also will be at different temperatures, changes in the thermal structure of the AVHRR will results in variable amounts of straylight and hence give rise to a time variable bias.

*Table 7 Effects tables for the thermal environment bias*

| Table descriptor | | |
|---|---|---|
| Name of effect | | Thermal environment bias |
| Affected term in measurement function | | $f(T_{Instr})$ |
| Instruments in the series affected | | All |
| Correlation type and form | **Pixel-to-pixel [pixels]** | Rectangular Absolute |
| | **from scanline to scanline [scanlines]** | Rectangular Absolute |
| | **between images [images]** | N/A |
| | **Between orbits [orbit]** | Rectangular Absolute |
| | **Over time [time]** | Truncated gaussian |
| Correlation scale | **Pixel-to-pixel [pixels]** | $\left[-\infty, +\infty\right]$ |
| | **from scanline to scanline [scanlines]** | Function relating to solar contamination modelling. |
| | **between images [images]** | N/A |
| | **Between orbits** | For orbits close in time there will be a 100% correlation in the |

| | [orbit] | error ($T_{Instr}$ won't change between close orbits). On daily timescales will be assessed from the curve of $T_{Instr}$ as a function of time |
|---|---|---|
| | Over time [time] | Correlation will drop off over time with a typical sigma of a year |
| Channels/ bands | List of channels / bands affected | All IR channels |
| | Correlation coefficient matrix | N/A |
| Uncertainty | PDF shape | Gaussian |
| | units | W m$^{-2}$ sr$^{-1}$ |
| | magnitude | A model of the uncertainty will be provided based on the final statistics relative to a matchup dataset |
| Sensitivity coefficient | | $\dfrac{\partial L_E}{\partial T_{instr}}$ |

Without a full thermal model of the AVHRR and also given that the number of temperature measurements available are small, especially for the early sensors where the IWCT temperature is pretty much the only temperature available, $T_{Instr}$ is the only indicator as to thermal state that is available across all AVHRRs. We therefore attempt to model the thermal environment bias as a function of $T_{Instr}$. Previous studies (e.g. Mittaz et al. 2013) have shown that the form of the bias dependence can have a time dependence in that different time periods can have distinctly different $T_{Instr}$ vs bias behaviours so the model to describe the bias can be both complex and temporally variable. The plot below shows the sort of behaviour seen in the AVHRR/1 and AVHRR/2 sensors where sometimes a linear model works, sometimes a more complex model is needed. For NOAA-14 three different separate models were needed which cover different time periods and are denoted in different colours.
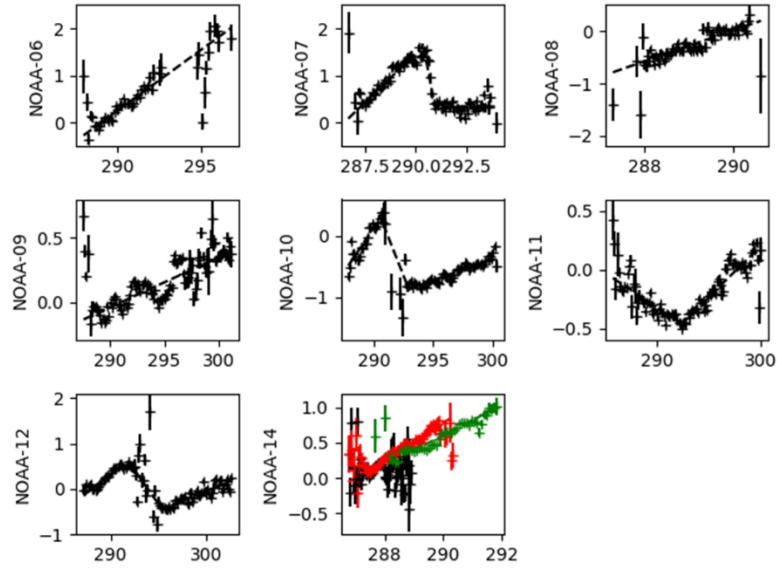
*Figure 3 $T_{Instr}$ versus bias (relative to an RTM modelled radiance) for a range of AVHRRs. Plotted is the $T_{Instr}$ (x-axis) against bias (y-axis). The plots show the range of different behaviour seen across different AVHRRs. For NOAA-14 the different colours correspond to different time periods (see Appendix for more detail)*

In terms of the correlation structure the current model calculated the bias on the basis of an orbital average temperature (note that the within an orbit bias terms are dealt with elsewhere). Therefore, within a single orbit there is just a single bias value and so all pixels have a 100% correlated error structure. On the timescale of one orbit to the next the value of $T_{Instr}$ will not change significantly so again on the timescale of a day the correlation structure will be close to 100% but this can be assessed from timeseries of $T_{Instr}$.

## 4.6  Emissivity

Note that there is no uncertainty associated with $\varepsilon$. This is because any error in this term will be corrected for by the harmonisation process.

## 4.7  Model assumptions

The +0 term in the main equation, Eq 3-2, considers the following effects:

- Non-quadratic nonlinearity
- Variable nonlinearity coefficient

The model equation assumes that the quadratic function fully describes the conversion from counts to radiance. For the HgCdTe detector (for the 11 μm and 12 μm channels), this may not be the case. Physically the nonlinearity is thought to be dominated by Auger recombination which is itself related to the lifetime of semiconductor carriers. As the total number of carriers changes, the Auger recombination rate changes and at higher carrier numbers suppresses the number of effective carriers reducing the observed current. The exact details of the non-linear behaviour is then related to doping levels, lattice defects etc. in the detector and is not expected to be strictly quadratic. The first effect table is then to do with the non-quadratic nature of the nonlinearity. Because we cannot measure the effect in detail from the pre-launch measurements and we do not have access to the original manufactures data we cannot know exactly what errors may be introduced by assuming a simple quadratic. We are then left with a Type-B uncertainty estimate (expert judgement, see Appendix A.4).

The second effect table is related to the fact that the nonlinearity of an HgCdTe detector is not itself a constant even though the AVHRR measurement equation assumes that it is. Again, this is a case where there is experimental evidence of the variation in the nonlinearity (see for example Theocharous & Theocharous 2006) but for which estimates for the impact in the case of the detectors flown on-board the AVHRR sensors will be difficult if not impossible to directly measure. Again we have to use a Type-B estimate and cannot fold this effect into our measurement equation directly due to lack of information. This is described in more detail in Appendix A.4.

*Table 8 Effects tables for the non-quadratic and variable nonlinearities*

| Table descriptor | | | |
|---|---|---|---|
| Name of effect | | Non-quadratic nonlinearity | Variable nonlinearity coefficient |
| Affected term in measurement function | | +0 | +0 |
| Instruments in the series affected | | All | All |
| Correlation type and form | **Pixel-to-pixel [pixels]** | Rectangular Absolute | Rectangular Absolute |
| | **from scanline to scanline [scanlines]** | Rectangular Absolute | Rectangular Absolute |
| | **between images [images]** | N/A | N/A |
| | **Between orbits [orbit]** | Rectangular Absolute | Rectangular Absolute |
| | **Over time [time]** | Rectangular Absolute | Rectangular Absolute |
| Correlation scale | **Pixel-to-pixel [pixels]** | $[-\infty, +\infty]$ | $[-\infty, +\infty]$ |
| | **from scanline to scanline [scanlines]** | $[-\infty, +\infty]$ | $[-\infty, +\infty]$ |
| | **between images [images]** | N/A | N/A |
| | **Between orbits [orbit]** | $[-\infty, +\infty]$ | $[-\infty, +\infty]$ |
| | **Over time [time]** | $[-\infty, +\infty]$ | $[-\infty, +\infty]$ |
| Channels/ bands | **List of channels / bands affected** | 11 µm, 12 µm | 11 µm, 12 µm |
| | **Correlation coefficient matrix** | Diagonal matrix | Diagonal matrix |
| | **Covariance** | | |
| Uncertainty | **PDF shape** | Gaussian | Gaussian |
| | **units** | $W\ m^{-2}\ sr^{-1}$ | $W\ m^{-2}\ sr^{-1}$ |
| | **magnitude** | Single value provided | Single value provided |

| Sensitivity coefficient | $\dfrac{\partial L_{\mathrm{E}}}{\partial L_{+0}} = 1$, | $\dfrac{\partial L_{\mathrm{E}}}{\partial L_{+0}} = 1$ |
|---|---|---|

# 5  Harmonisation

Harmonisation across the sensor series for FIDUCEO project purposes is described separately, so only a brief overview is considered here. The harmonisation coefficients represent the nonlinearity of the instrument (note this is distinct from the nonlinearity of the detector itself due to nonlinearities in the electronics as well as nonlinearities introduced due to SRF issues), the bias due to straylight differences between the calibration and observation views and an emissivity correction respectively.  Note that the parameters

- $a_0$: As shown in Mittaz et al. (2009) this term arises from differences in the straylight between the Earthview position and the spaceview position.
- $a_1$: A correction factor to the emissivity term. This is needed in part because the only value for the emissivity for the AVHRR was a theoretical estimate only. This terms also partially corrects for problems with variable gradients across the IWCT in an average sense (Mittaz et al. 2009).
- $a_2$: The instrument nonlinearity. This is caused both by the native nonlinearity of the detector as well as nonlinearities due to the on-board electronics. There will also be a component which will partially correct for differences between the assumed and true spectral response function.
- $a_4$: A harmonization term needed to align the thermal environment bias model with the true instrument behaviour

The harmonisation process will determine these parameters, and a covariance matrix for the parameters. To propagate these uncertainties through to the uncertainty associated with the Earth radiance we need the sensitivity coefficients:

$$\frac{\partial L_{\mathrm{E}}}{\partial a_0} = 1 \ . \qquad\qquad Eq\ 5\text{-}1$$

$$\frac{\partial L_{\mathrm{E}}}{\partial a_1} = \frac{\tilde{L}_{\mathrm{IWCT}}\left(\bar{C}_{\mathrm{S}} - C_{\mathrm{E}}\right)}{\left(\bar{C}_{\mathrm{S}} - \bar{C}_{\mathrm{IWCT}}\right)} \ . \qquad\qquad Eq\ 5\text{-}2$$

$$\frac{\partial L_{\mathrm{E}}}{\partial a_2} = \frac{-\left(\bar{C}_{\mathrm{S}} - C_{\mathrm{E}}\right)}{\left(\bar{C}_{\mathrm{S}} - \bar{C}_{\mathrm{IWCT}}\right)} \qquad\qquad Eq\ 5\text{-}3$$

$$\frac{\partial L_{\mathrm{E}}}{\partial a_3} = -\left(\bar{C}_{\mathrm{S}} - \bar{C}_{\mathrm{IWCT}}\right)\left(\bar{C}_{\mathrm{S}} - C_{\mathrm{E}}\right) + \left(\bar{C}_{\mathrm{S}} - C_{\mathrm{E}}\right)^2 \qquad\qquad Eq\ 5\text{-}4$$

$$\frac{\partial L_{\mathrm{E}}}{\partial a_4} = f\left(T_{\mathrm{inst}}\right) \qquad\qquad Eq\ 5\text{-}5$$

Note that the harmonisation coefficients will be correlated with each other and the result of the harmonisation process will include a covariance matrix for these. Therefore to propagate

uncertainties, the full law of propagation of uncertainties, including the correlation term, is required. Note that the harmonisation coefficients will be the same for all time with one sensor and there will be a correlation between different sensors in the FCDR series because of correlations between harmonisation coefficients over these longer timescales.

# A    Appendix on detailed information about uncertainty components

## A.1    Noise and cross talk, correlations observed

Noise can arise in a number of different physical process. There will be noise from the detector itself which can be related to a range of physical causes including but not limited to thermal noise (itself related to the detector temperature), shot noise (related to the number of photons hitting the detector at any one time) etc. There will also be noise from the electronics which often will have a characteristic noise spectrum of *1/f*. And there can also be cross-talk where either an extraneous signal is introduced into the observed signal or one channels signal can cross over and contaminate another channel. This latter effect will give rise to correlations between channels.

In the case of the AVHRR all of the above effects have been seen, In particular the 3.7µm channel has shown a strong time dependent noise term which has a noise spectrum close to *1/f* (e.g. Mittaz 2016). This indicates that much of the noise in the 3.7µm channel arises in the electronics and there is further support for this from the AVHRR on TIROS-N. In the case of TIROS-N it has been known since it was launched that the noise was highly variable within an orbit and this was fixed in subsequent AVHRRs by changing the design of the electronics. TIROS-N also shows evidence for a strong cross-talk signal which again was significantly reduced when the electronics was redesigned.

To measure the noise for all channels we have first removed the many outliers that can occur. At the moment the outlier information is based on simple thresholds and works well as will be shown below. The thresholding has a significant impact on both the measured signal as well as the noise estimates (see below). We have used the Allan deviation to generate the statistics as this allows us to calculate the noise for both space and IWCT views in the same way (for more details see Mittaz 2016).

### A.1.1    Visible channels

While we are not recalibrating the visible channels we are including them in our FCDR so they need uncertainty estimates. Because we are not recalibrating these channels we cannot do a full uncertainty analysis but we can include some components of the uncertainty. First is the Allan deviation from an orbits worth of data which represents the uncertainty caused by random effects. Second is a systematic component of uncertainty related to the uncertainties in the calibration coefficients used to generate the visible channel data which is based on the visible channel coefficients taken from the CSPP (Community Satellite Processing Package) package which is itself based on the PATMOS-X calibration (e.g. Heidinger et al. 2010). Note that the visible channels do not have any on-board calibration system so the updates to the calibration are done vicariously.

Figure 4 shows both the noise and mean values of the space (dark) counts for the 0.6µm channel on NOAA-09 and shows both the importance of filtering on both the noise and mean estimates as well as the fact that the noise itself is time variable. These estimates will be included in the FIDUCEO FCDR.

For the uncertainty due to systematic effects this will be based on estimates of the uncertainty of the visible channel calibration process. The quoted estimates from Heidinger et al. (2010) are 2%,3% and 3% for the 0.6µm, 0.8µm and 1.6µm channels. However, a preliminary analysis of the difference between multiple versions of the PATMOS-X calibration as well as compared to another independent estimate from NASA (NASA LaRC FCDR Doelling, D., Minnis, P., and the NOAA CDR Program (2015)) shows differences of the order of 3%, 5% and 5% (sometimes much larger) so we will be using these updated estimates of the uncertainty for the non random component of uncertainty in the easy FCDR.
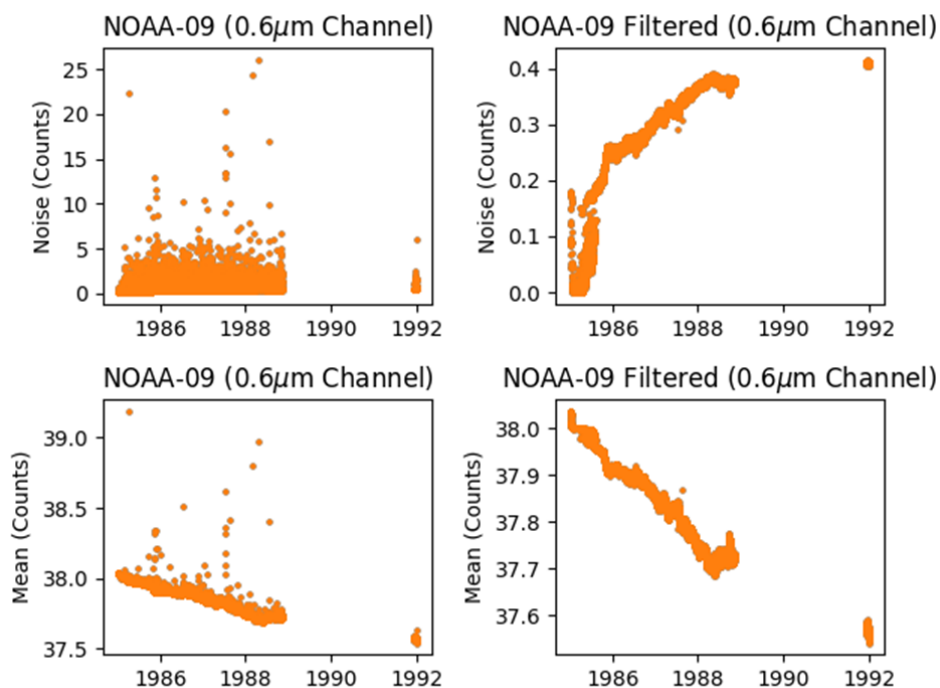


*Figure 4 Noise and mean counts from NOAA-09 0.6 micron channel. The left hand column shows the estimated noise and mean value before filtering and the right hand column shows the same after filtering. So both a filtered dataset and a variable noise are needed to correctly use the AVHRR visible channel data.*

### A.1.2   IR Channels

The filtering and noise estimates are the same for the IR channels. Again we see time dependent variations and also note the importance of filtering on the data. Figure 5 shows an example for NOAA-07 where the noise increases to a large value for the 3.7µm channel and then drops back down abruptly at the end of September 1983. At this point the instrument was outgassed and the IR sensors were turned off effectively resetting everything. This behaviour therefore indicates that the noise is not dependent on the physical state of the detector or of the incident flux levels but is related to something else on-board such as the electronics. This is also supported by the fact that for the AVHRR/3 sensors the electronics were redesigned and similar noise patterns were not seen. **Error! Reference source not found.** also highlights the spectral variability of the AVHRR noise. As for other sensors as stated above, TIROS-N is a special case as the noise varied significantly around the orbit with something approximating to a day/night variation.
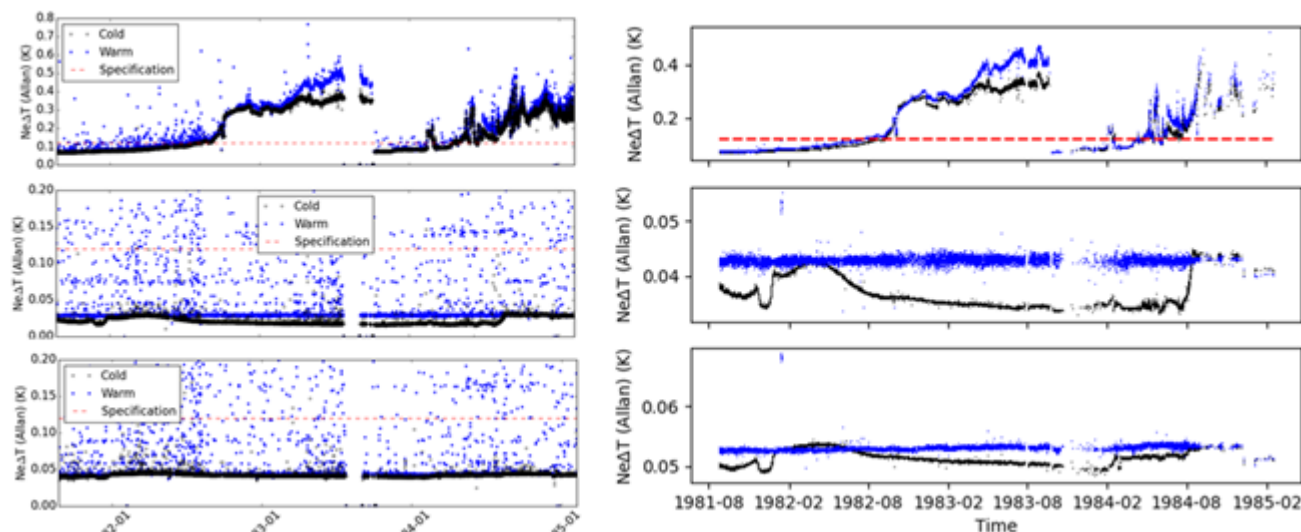
*Figure 5 Space view (black) and ICWT noise (blue) estimates for NOAA-07. The left hand column shows the pre-filtered data, the right hand column shows the data after filtering. The red dotted line is the pre-flight specification. The 3.7µm channel noise (top panels) is highly variable with a step jump seen in late 1983. This was caused by an outgassing event that turned off the IR channels for an extended period and illustrates how the noise is not just from the detector but is influenced by the electronics/spacecraft as well. The 11 µm channel noise (middle panel) and the 12 µm channel noise (lower panel) are more stable.*

In terms of noise covariance across the channels and scanning positions, for the space view and for the ICT, some evidence of cross-talk has been found in the older instruments in the sensor series. In Figure 7, the correlation with scanline position for the space view shows strong correlation with neighbouring scanline positions in the case of Channel 3b of TIROS-N. For IR channels 4 and 5, there is strong cross-talk in the first five positions. The older NOAA-07 also presents cross-talk (albeit with some block structure) in the space view in channel 3b but channels 4 and 5 do not show any strong cross-talk effect.

| AVHRRTN_G, 1978-12-12 | AVHRR07_G, 1982-09-01 | AVHRR18_G, 2010-12-01 | |
| --- | --- | --- | --- |
| space count corr / position | space count corr / position | space count corr / position | |
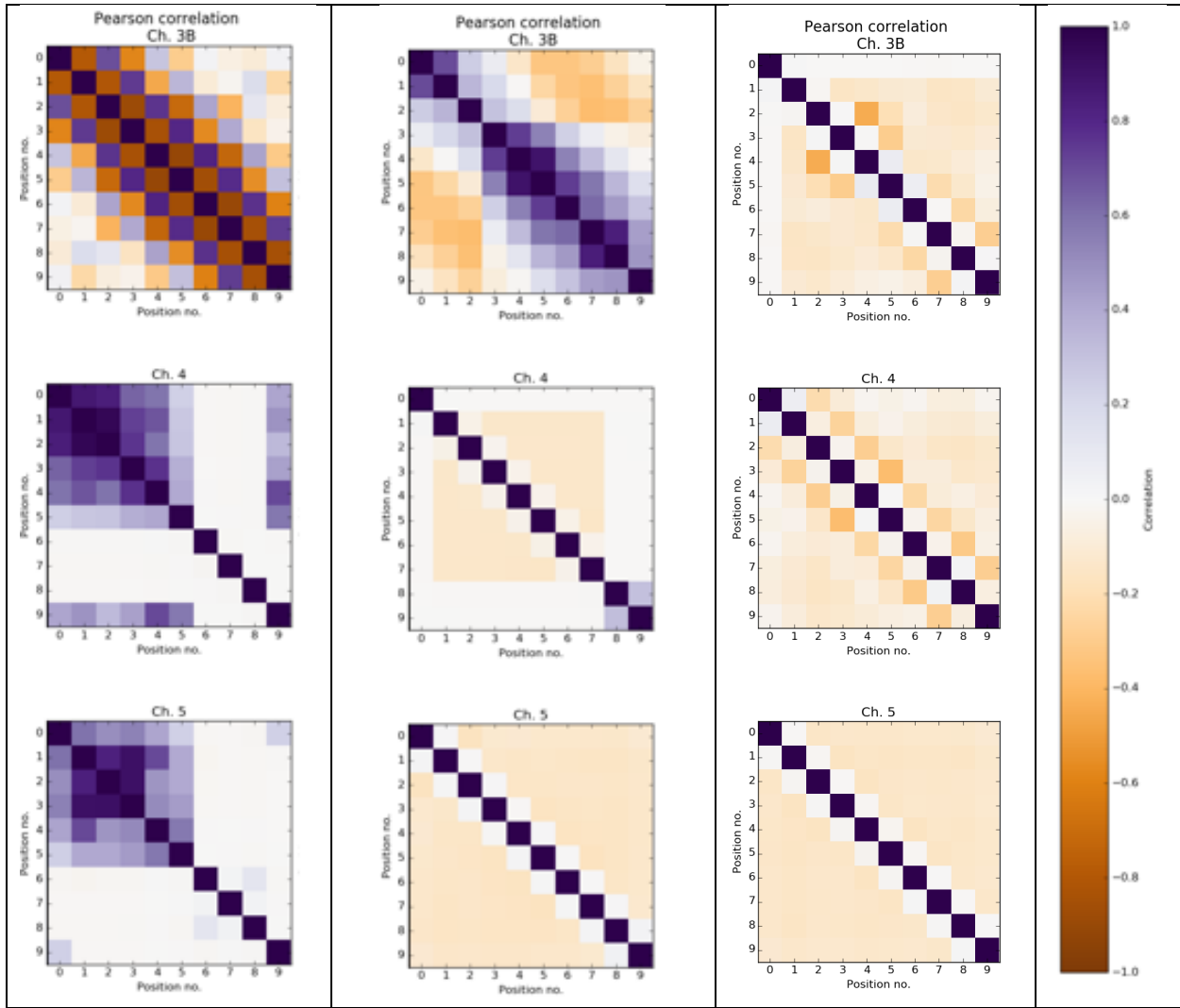
*Figure 6 Space view noise correlations between reflectance channels for TIROS-N, NOAA-07 and NOAA-18. The Pearson product-moment correlation is shown.*

A similar picture is painted by ICT noise correlations with scanline position in Figure 7. Strong cross-talk is evident for TIROS-N on channel 3b. Some localized cross-talk and a block structure is observable for channel 5 (channel 4 looks more free of cross-talk). NOAA-07 and NOAA-18 exhibit similar phenomenology to the space view case with correlations across scanline positions in the case of channel 3b and little or no evidence of cross-talk in channels 4 and 5.

| AVHRRTN_G, 1978-12-12 | AVHRR07_G, 1982-09-01 | AVHRR18_G, 2010-12-01 | |
|---|---|---|---|
| ict count corr / position | ict count corr / position | ict count corr / position | |
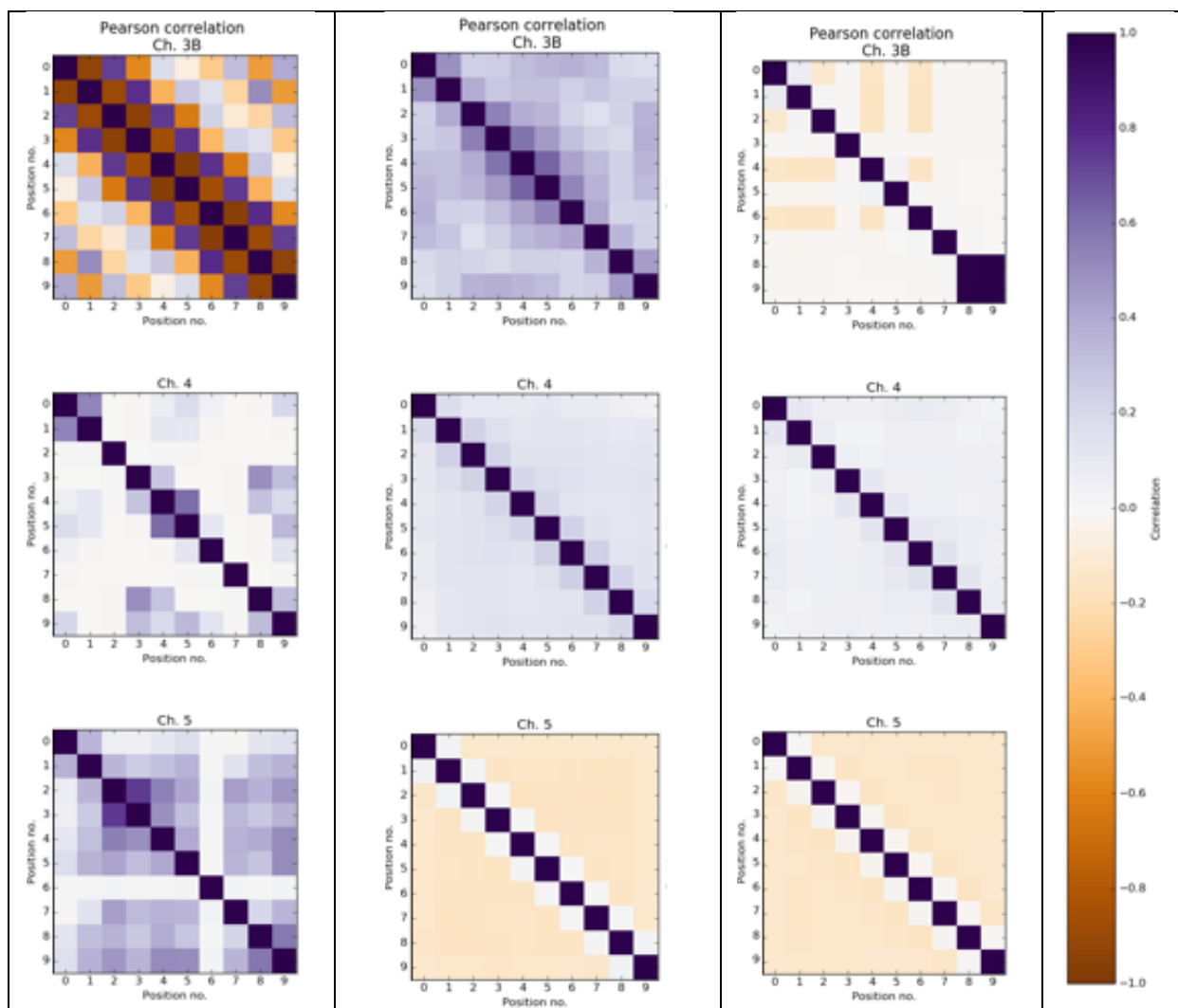
*Figure 7 ICT noise correlations between reflectance channels for TIROS-N, NOAA-07 and NOAA-18. The Pearson product-moment correlation is shown.*

This suggests that the cross-talk issue has been addressed in the sensor series post-1982 especially for the two IR channels 4 and 5.

## A.2 Spectral response function biases

The errors caused by spectral response differences have yet to be included in our current FCDR but will be studied in the future. With the current work there will be some correction for possible SRF errors because as already mentioned, the nonlinearity term in the harmonisation ($a_2$) will correct for some SRF problems.

## A.3 Internal warm calibration target (IWCT) effects

### A.3.1 PRT noise

Within FIDUCEO, we have performed a detailed study of the PRT noise which appears to be constant over time and for all versions of the AVHRR. Its value is close to 0.3 counts or 0.015 K as can be seen in Figure 8 for NOAA-07 below.
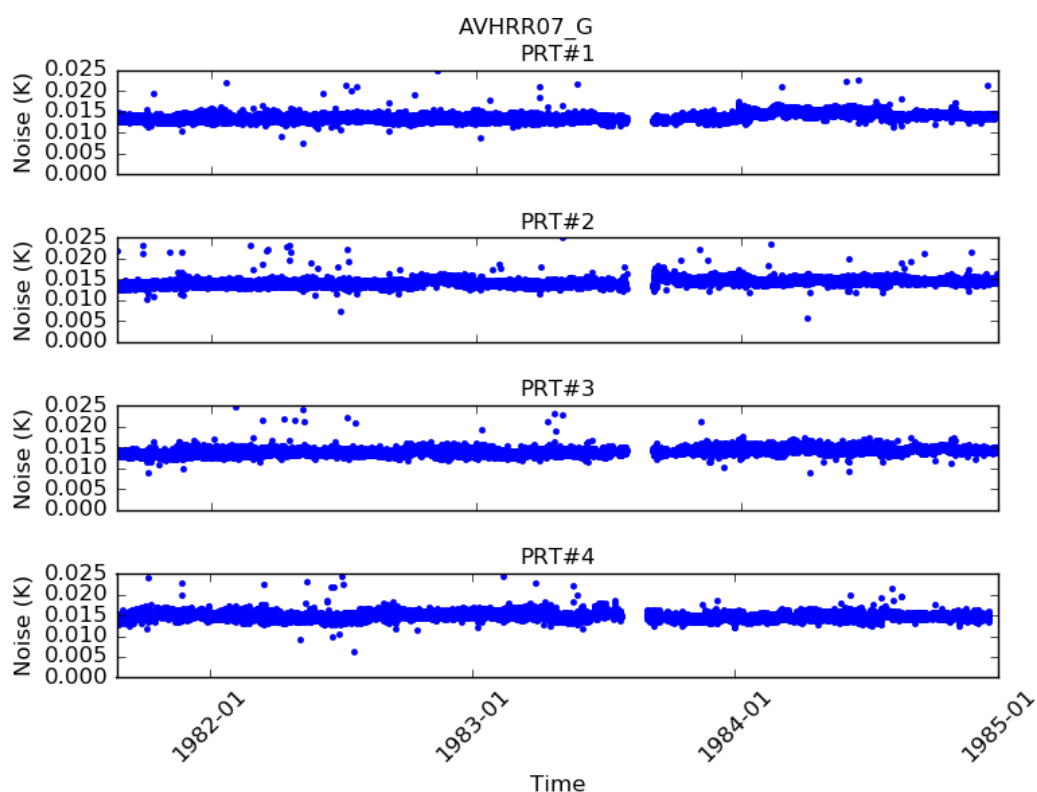
*Figure 8 Noise of the four individuals PRT for NOAA-07, in temperature. The noise is estimated by calculating the Allan deviation of all the PRT measurements over an orbit.*

### A.3.2   Thermal gradients across the IWCT

Because the IWCT on the AVHRR is not a sophisticated blackbody and should rather be seen as observing a portion of the instrument blackbody, other effects come into play. Thermal gradients across the IWCT are not controlled and only four PRTs were used to measure its temperature (which is insufficient to reliably detect complex thermal gradients across its surface if present). This means that lack of knowledge of such gradients will give rise to an uncertainty on the final IWCT radiance.

An estimate of the size of such non-uniformities can be made if we assume that the PRTs are equidistant from each other. We can then fit a simple plane to three of the PRT temperatures and see if the fourth is consistent with the other three. If it is, then gradients across the IWCT are not a problem. Figure 9 shows that the distribution of the difference between the measured PRT temperature and the PRT temperature deduced from the 3 others, for three days selected to represent three different epochs of AVHRR behaviour.  It is apparent from Figure 9 that not only it is likely that an assumption of a uniform temperature gradient across the IWCT is wrong, but that there is also a time-dependent component.
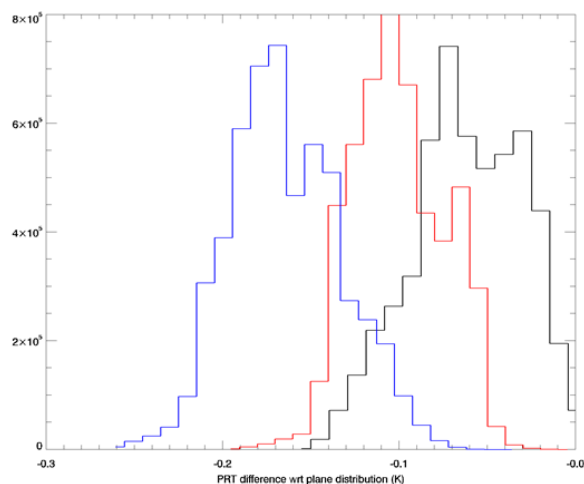
*Figure 9a Difference between a planar temperature distribution over the ICT and a measured value for three epochs (01-01-2003, 01-01-2004 and 01-01-2009) for NOAA-16. Not only is the assumption of a planar distribution not met, but the average gradient also change*

Furthermore, the ICT error arising from such gradients will apply to all IR channels. While such gradients also appear in other instruments and their impact is time dependent and related to orbit drift, this will need assessing for all sensors with on-board calibration. There is currently no way to estimate the bias due to this effect but using the matchup data together with the Harmonisation a 'strong gradient present' bias will be parameterised.

To get a feeling for the correlation scale associated with modelling the thermal gradient with a planar model, we calculated the anomaly between the measured value of PRT4 and the expected value from a linear fit through the other 3 PRTs for a range of cases. In particular, we investigated the variation of the PRT anomaly along scanlines and across orbit (i.e. on various temporal scales) for the AVHRR/3 sensor onboard NOAA-18, and also for the AVHRR/1 sensor onboard NOAA-8 and the AVHRR/2 sensor onboard NOAA-7. This choice caters for both morning and afternoon equatorial crossings, and also allows for a comparison of the AVHRR/3 sensor that has implemented a sun shield.

In order to ensure consistency between plots, we used the Haversine formula for great circles on a spherical Earth and integrated the central angle with respect to equatorial crossing time. This 'distance' measured in angular radians is invariant in the time domain and is calculated directly from geolocation via the latitudinal and longitudinal coordinates.

For each sensor we have selected a baseline day and calculated the PRT anomaly for all scans that day to 1) assess the typical variability and hence potential correlation structure along a scanline and 2) to assess correlation with neighbouring scanlines. We then also selected orbits at approximately midnight on different days at the daily, monthly, yearly and multi-year timescale.  Figure 10b presents the results of this sampling approach across the 4 aforementioned sensors.

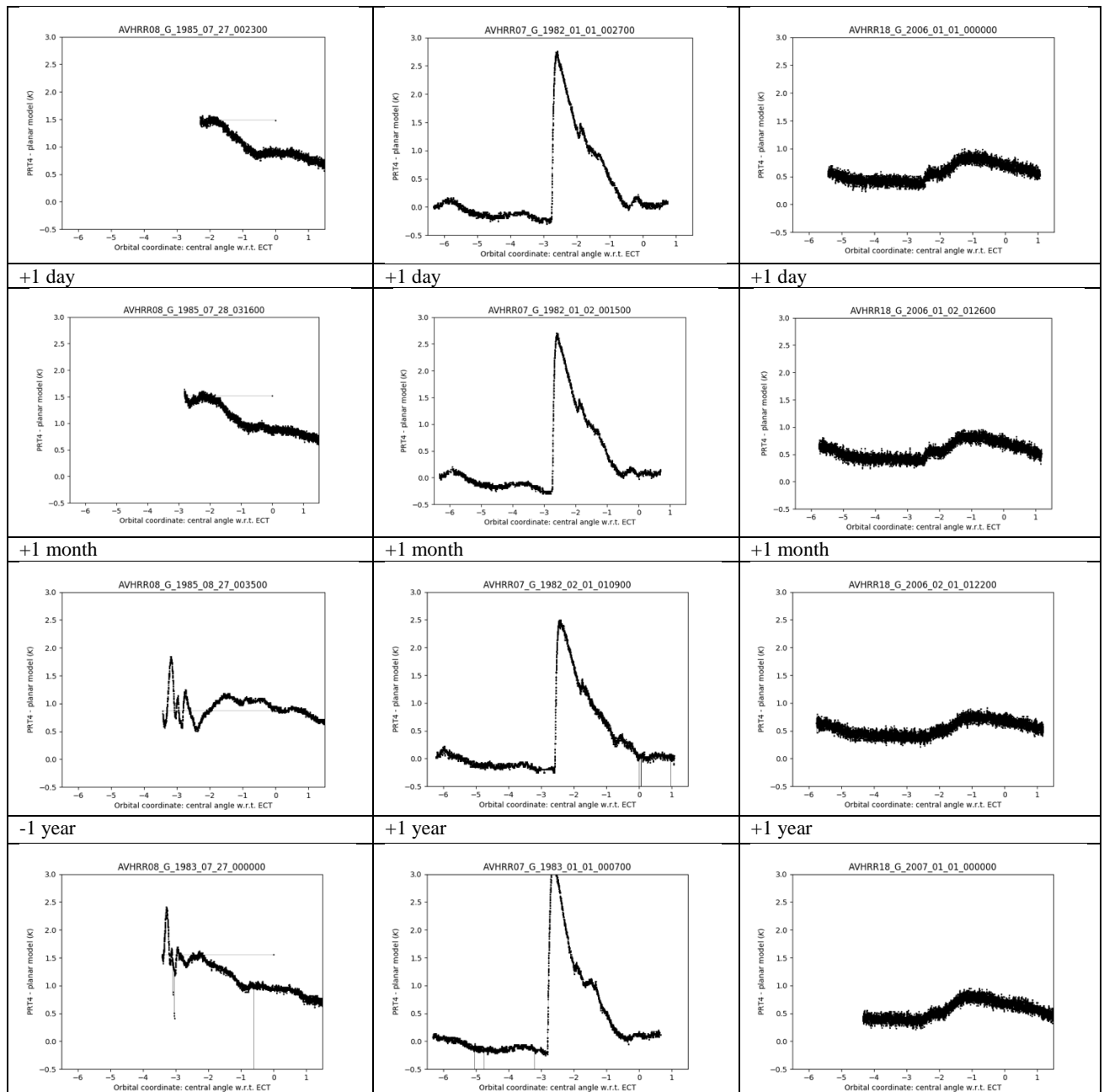| NOAA-8 (AVHRR/1 AM) | NOAA-7 (AVHRR/2 PM) | NOAA-18 (AVHRR/3 PM) |
|---|---|---|
| 27.07/1985 | 01/01/1982 | 01/01/2006 |

*Figure 10b Variation of the PRT4-planar model scanline anomaly for the AVHRR/3 sensor NOAA-18 and the non-AVHRR/3 sensors NOAA-8 and NOAA-7 over a range of temporal lags with respect to the first scanline plot.*

Very different correlation structures can be observed for the AVHRR/1, AVHRR/2 and AVHRR/3 sensors. On 27 July 1985, the AVHRR/1 sensor onboard NOAA-8 presents a scanline PRT4–planar model anomaly structure that is similar on the daily scale but shows strong variability a month later. The total variability along the scanline is of the order of 1-1.5K. One year on, the behavior is starting to bear closer resemblance again to the initial case suggestive perhaps of an annual cycle.

In the case of the AVHRR/2, solar contamination leads to a change in anomaly of the order of 1.5-2.0K over all scales but either side in a 1-hr temporal interval, approximately constant anomaly is observed. We interpret these flat near-zero regions as indicative of the planar assumption being valid there. Contrary to AVHRR/1, the PRT anomaly structure shows strong resemblance up to the yearly timescale – suggestive of a longer-term correlation structure for this sensor. We will quantify

this stable correlation structure (that is present both in neighbouring scanlines and across-orbits for the AVHRR/2) and provide a function for the correlation scales involved.

Very different anomaly time series are observed in the case of the AVHRR/3 sensor that has a sun shield in place. The traces appear broadly more sinusoidal in form and there is little or no visual evidence of strong solar contamination. This is true over neighbouring scanlines and over the multiple timescales considered here. In the AVHRR/3 plots the scanline anomaly also appears to be somewhat lower in magnitude.

Work is ongoing to quantitatively assess the scanline anomaly functional forms as well as their cross-correlation over a range of temporal scales. As mentioned earlier, we will classify the range of PRT anomaly correlation structures and their timescales using time series statistics including the cross-correlation in the next reporting period.

### A.3.3   Solar contamination

At the moment the operational gain calculation (for the 3.7 µm channel) identifies peaks in the gain due to sunlight reflected off the ICT and "chops them off" using a detection and fitting procedure that has been applied since November 1995. Figure 11 shows an example of the implementation of this method to the 3.7 µm channel of NOAA-14. There is an uncertainty associated with this correction related to the interpolation across the filtered section of the time series into the region of the tail of detected peaks.
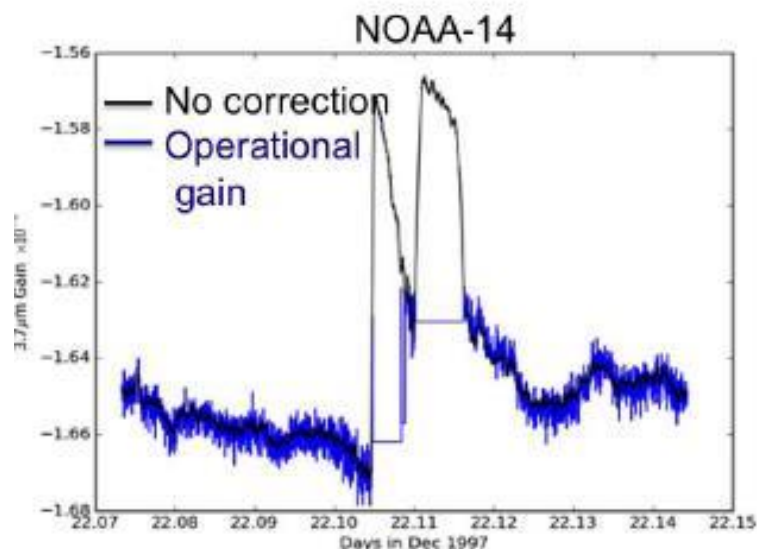


*Figure 11 Detection of a solar contamination event in the 3.7 µm channel of NOAA-14 and the corrected operational gain obtained by interpolation of the filtered signal. Note that this procedure introduces an uncertainty associated with interpolation across filtered portions of the time series into the region of the tail of each peak.*

There are two improvements that are planned to reduce the impact of the solar contamination. The first is to have a new solar contamination detection algorithm which would be similar to the current operational algorithm shown in Figure 11. This is needed because operationally the detection of solar contamination effects was only introduced in 1994 which means that all the early AVHRRs have had no solar contamination detection applied at all. The introduction of the operational algorithm is clearly shown in Figure 12.
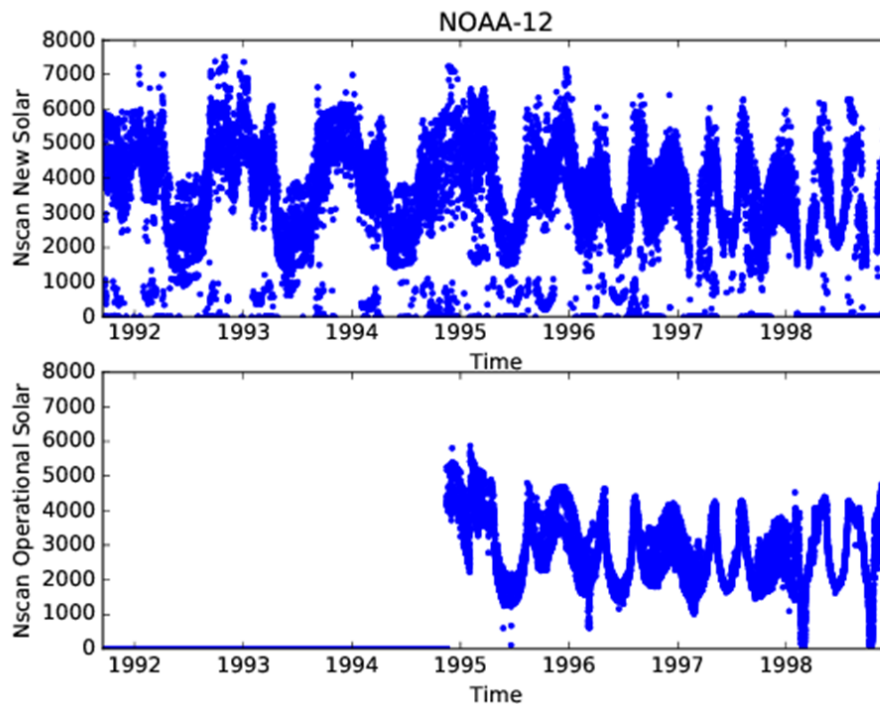
*Figure 12 A comparison of the new solar contamination algorithm showing the number of scanlines detected per orbit as a function of time compared with the operational algorithm. There are two things of note. First, the 'turn on' of the operational detection algorithm can be clearly seen and shows that all AVHRR data before late 1994 will have not accounted for the solar contamination at all. Second, the new algorithm detects more scan lines.*
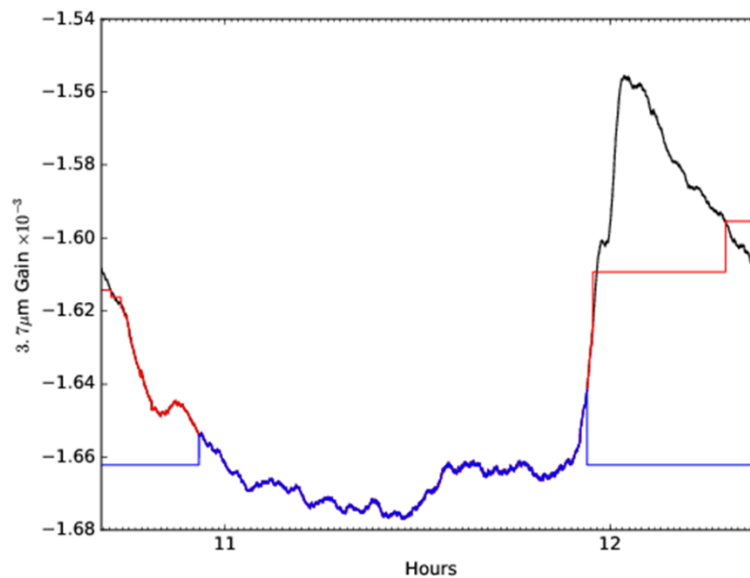


*Figure 13 One orbit for NOAA-12 showing the new algorithm (in blue) detects more of the solar contamination event than the operational algorithm (in red). In this case half the orbit is actually impacted by the solar contamination.*

Figure 13 shows the difference between the new and old algorithm at the orbit level. The blue line shows the new algorithm and the red the old and it can be seen that the old algorithm misses a lot of the apparent solar contamination. Therefore the new algorithm works both for the pre-1995 data as well as being an improvement over the old algorithm when present.

The other issue with the operational algorithm is that when a solar contamination event was detected it just used a constant value for the gain rather than a variable value which would be expected. Because we see some gain variability as a function of time which is for the 3.7µm channel is likely due to a nonlinearity in the electronics rather than in the detector (for the 11µm and 12µm channel there is detector nonlinearity as well which will dominate) we can use this to estimate what the gain should be More specifically, the model assumes then that the squared gain is expected to be proportional to the self-emission of the instrument and therefore the ICT radiance as follows:

$$\left[ \frac{(\varepsilon + a_1)R_{ICT} - a_2(C_s - C_{ICT})^2}{(C_s - C_{ICT})} \right]^2 = Gain^2 \propto a_2 R_{self}$$

such that the ICT radiance is effectively acting as a proxy for the instrument temperature.

Figure 14 shows a plot of the squared gain versus the ICT radiance for three orbits. The straight line fit represents that part of the orbits where the sun is not shining on the ICT, clearly distinguishable from a different behaviour where the sun is shining on the ICT. The red portion of this region shows the part captured by the solar contamination detection routine and the difference between the upper linear fit line and a lower linear (parallel) fit at the "shoulder region" is likely to be a good indication of the uncertainty associated with this correction (of the order of ~0.005 mW$^{-2}$ sr$^{-1}$ cm$^{-1}$). The negative slope of the dependency is due to the negative slope of the small nonlinearity due to the electronics.

Importantly, this method is also applicable to the 11 µm and 12 µm channels. The gain model also means that it is possible to estimate the gain at any time for any of the IR channels and therefore estimate the radiance seen from the ICT based on the observed counts as shown in the right hand panel of Figure 14.
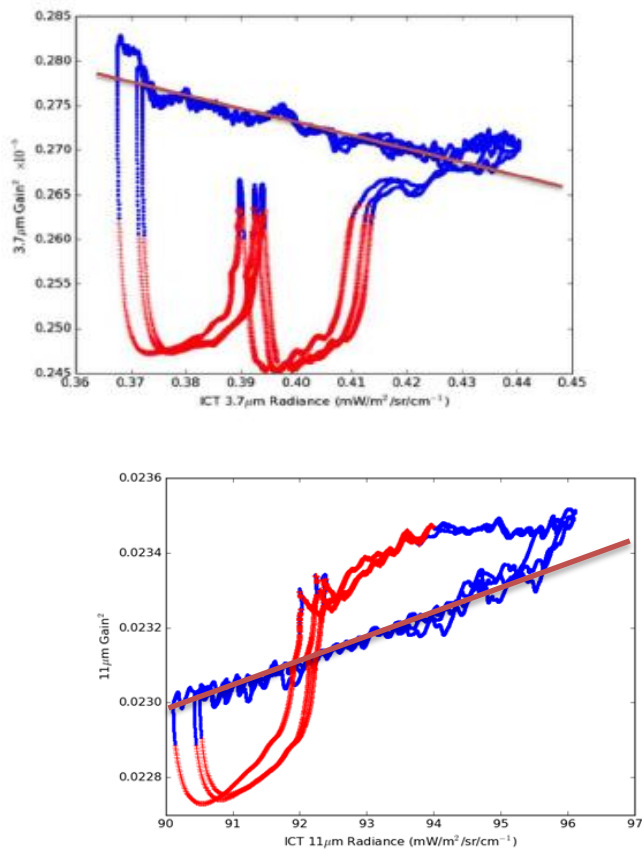
*Figure 14 Detection of two solar contamination events in the 3.7 μm channel of NOAA-14 and the corrected operational gain obtained by interpolation. (right) Estimation of the radiance seen by the ICT based on observed counts using the gain model for the case of the 11 μm channel of NOAA-14.*

Figure 15 shows how the model improves on the pre-November 1994 model shown in Figure 11 by not "flatlining" across the region impacted by solar contamination. The linear fits of Figure 14 (intercept and slope) then provide a quantitative measure of the size of the uncertainty of the new model's goodness of fit. While the approach is warrants more study, it offers a correction for the 11 μm and 12 μm IR channels that is currently not available. Correction of the scattered solar contamination is important in that it decouples this effect from those effects associated with thermal gradient effects across the ICT. Estimates of the sort of uncertainty that is available are also shown in Figure 15 by the dashed lines. These are based on the statistics of the fit relative to the data used to determine the gain model.
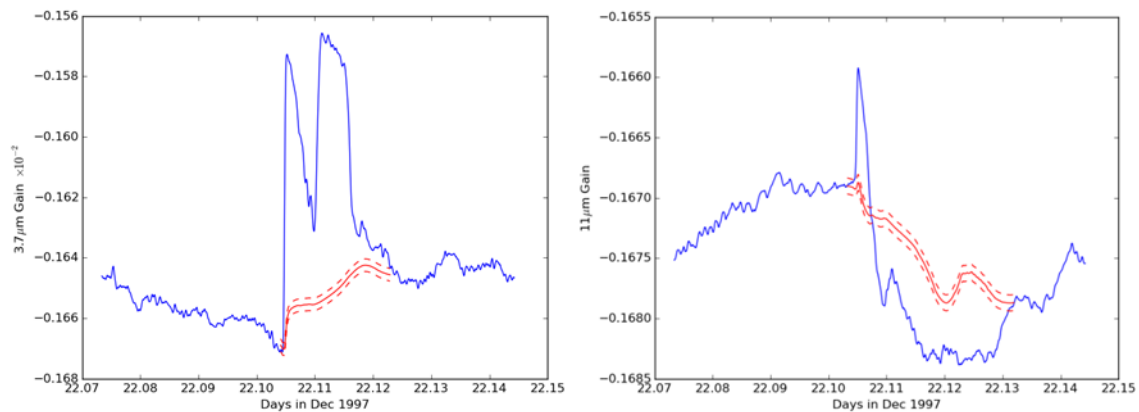
*Figure 15 Detection of solar contamination events in the 3.7 µm channel (left) and 11 µm channel (right) of NOAA-14 and the corrected operational gain obtained by interpolation with the new method.*

## A.4  Thermal environment bias effects

From Mittaz et al. (2009) it is known that the $a_0$ term in the measurement equation can be shown to be related to the difference between the straylight components present when looking at the Earth view and the space view. This then directly relates the original $a_0$ term to the thermal state of the AVHRR since the stray light will originate from certain (unknown) parts of the instrument body/optical train. Looking at it this way it is then clear that if the thermal environment of the AVHRR changes then the value of $a_0$ will also change. Given that there are long term changes in the Earth-Sun distance as well as in the AVHRR orbit itself (apart from the MetOp versions) we then expect a change in the AVHRR thermal state on long timescales.

We can see this by looking at the orbital average of IWCT temperature as a function of time. Figure 16 shows this for the AVHRR/3 sensors and shows a wide range of variability from NOAA-15 which for its whole life was subject to large temperature variations to NOAA-16 which shows distinct phases of variability to MetOp-A which shows small annular variations. The coloured lines at the top of some of the plots show where different time ranges have been defined for different models of the bias caused by the changes in the thermal environment. That different models are needed can be seen in Figure 16 where the bias between the NOAA-16 AVHRR and the AATSR sensors are shown for different time periods (the red and green times shown in Figure 16).
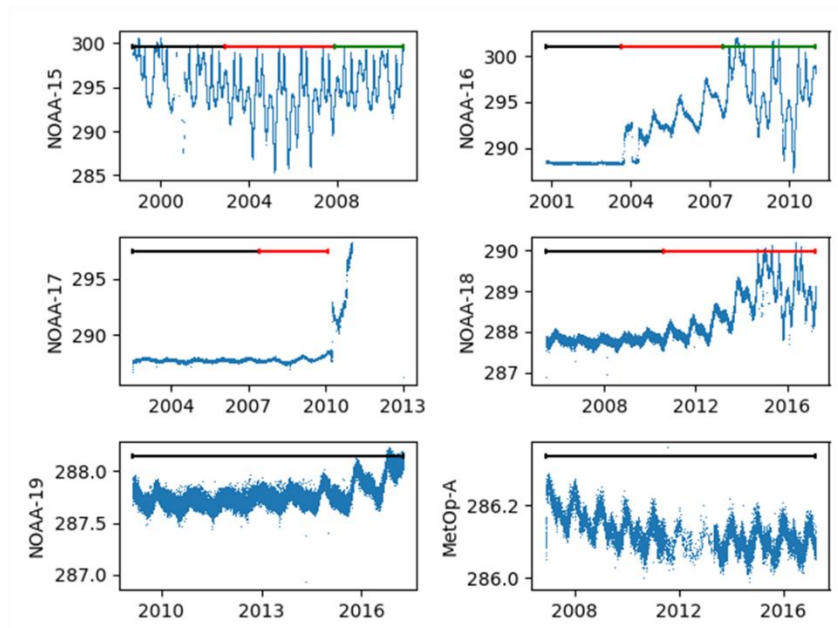
*Figure 16 The time variability of the orbital average temperature for the AVHRR/3 sensors. Note that there is a lot of variability which even includes MetOp-A which still shows an annual signal.*
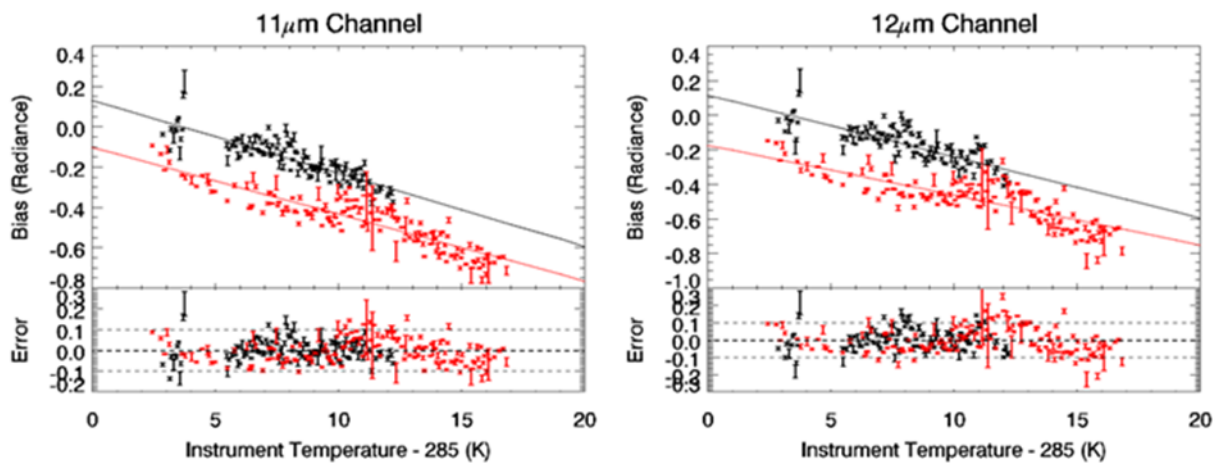


*Figure 17 Bias of NOAA-16 AVHRR vs the AATSR for two time periods defined by the red (the black symbols) and the green (red symbols) lines in Figure 16. The separation in both the 11µm and 12µm channels shows the need for two different models*

Currently we are investigating simple parameterisations of the instrument temperature vs bias dependence. Simple versions are shown in Figure 3 for the AVHRR/1 and AVHRR/2 sensors and in Figure 18 for the AVHRR/3 sensors. In both plots the colours where present refer to different time zones. An estimate of the uncertainty in the model will be based on the statistics seen when deriving the model itself, and there will be an extra uncertainty added though the harmonsation process.
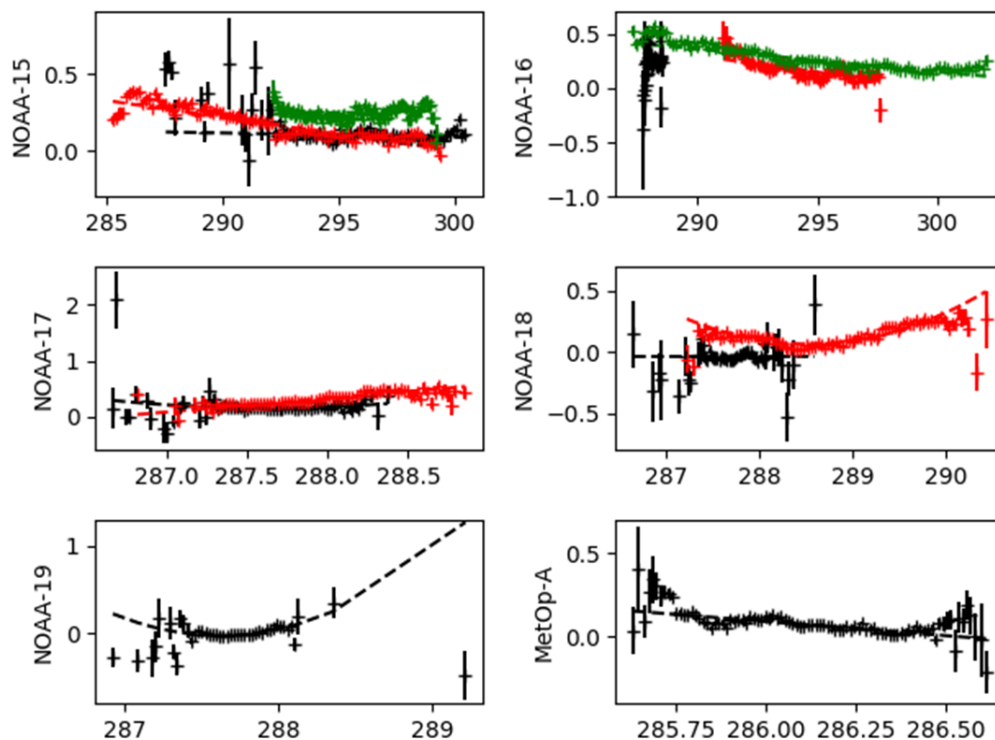
*Figure 18 Thermal environment bias (relative to RTM BTs) as a function of the instrument temperature for the AVHRR/3 sensors.*

## A.5 Model assumption effects

Table 6 presents two model assumption effects. The first is related to the non-quadratic nature of the nonlinearity and the second to the variability of the nonlinearity coefficient. Estimates of the scale of both effects have been derived from a numerical model of an HgCdTe detector based one used for the GOES Imager detectors (Bicknell 2000). The model determines the Auger recombination lifetimes of the carriers and hence variations in the predicted voltage seen for a given input photon flux and has been tuned to match the sort of photon fluxes and non-linearities seen in the AVHRR sensors. The top two plots of Figure 19 show the predicted deviation of the estimated brightness temperature using a quadratic measurement equation compared to the input brightness temperature and indicates that the quadratic assumption may be introducing and error of order a few milli-Kelvin, at least in terms of modelling the Auger recombination effect.
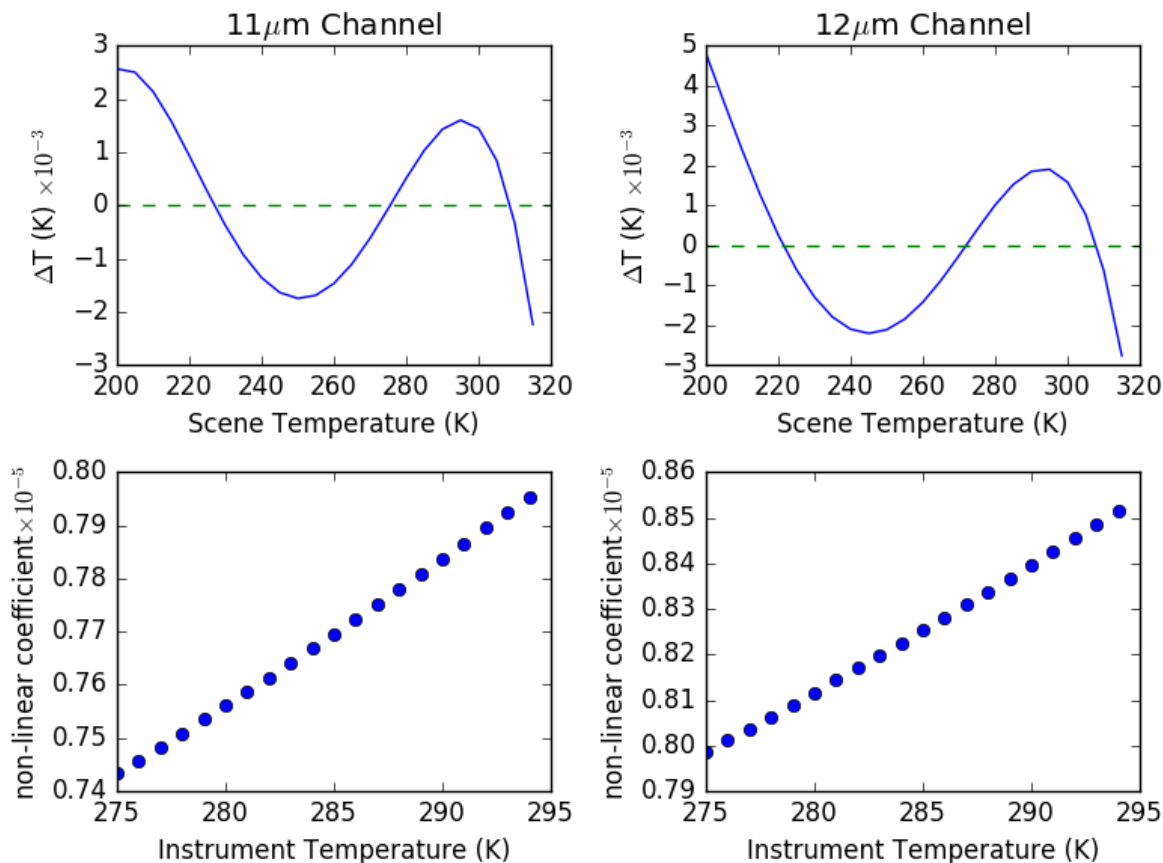
*Figure 19 Top two plots show the deviation from a quadratic model for an HgCdTe detector for the 11 and 12μm channels using a theoretical model. This indicates that the deviation from a quadratic are at the milli-Kelvin level. The two lower plots show changes in the quadratic nonlinearity coefficient as a function of instrument temperature (a proxy for the total self-emission radiance) and indicates for a typical AVHRR orbit a variation of ~1% change in the coefficient.*

The other nonlinearity effect that can be investigated using this model is the effect of the variable non-linear coefficient. To do this we have varied the self-emission component (parameterized by the instrument temperature) and tracked how the best fit quadratic term varies. This variation is shown in the lower panels of Figure 19 and shows over a 20 K variation in instrument temperature a variation of order 5% in the quadratic term. Given that a typical AVHRR shows orbital temperature variations more like ±1 degree this amounts to an approximately 0.4% change in the non-linear coefficient. For a 300K scene temperature and a typical instrument gain and nonlinearity this would correspond to an error of approximately ±0.006K which is of order the same size as shown for the non-quadratic error.

Both estimates will be included as part of the uncertainty budget of the final FCDR.